Model-Based Approach for Extracting Femur Contours in X-ray Images

CHEN YING

NATIONAL UNIVERSITY OF SINGAPORE

2005

Name: CHEN YING
Degree: Master of Science
Dept: Computer Science
Thesis Title: Femur Contour Extraction

Abstract

Extraction of bone contours from x-ray images is an important first step in computer analysis of medical images. It is more complex than the segmentation of CT and MR images because the regions delineated by bone contours are highly nonuniform in intensity and texture. Classical segmentation algorithms based on homogeneity criteria are not applicable. This thesis presents a model-based approach for either semi-automatically or automatically extracting femur contours from hip x-ray images. The semi-automatic method requires users to manually align the model to the femur in the image while the automatic method works by first detecting prominent features, followed by registration of the model to the x-ray image according to these features. Then the model is refined using active contour algorithm to get the accurate result. Experiments show that the semi-automatic method can always accurately extract the femur contours and the automatic method can extract the contours of the femurs with regular shapes, despite variations in size, shape and orientation.

Keywords: Contour extraction
Registration
Shape-constrained snake

Model-Based Approach for Extracting Femur Contours in X-ray Images

CHEN YING

(B. Sc. (Hon.) in Computer Science, NUS)

A THESIS SUBMITTED
FOR THE DEGREE OF MASTER OF SCIENCE
DEPARTMENT OF COMPUTER SCIENCE
SCHOOL OF COMPUTING
NATIONAL UNIVERSITY OF SINGAPORE
2005

Acknowledgments

First of all, I would like to sincerely thank my supervisor, A/Prof Leow Wee Kheng. He guided me all the way in my master years. He gave me countless precious advice and helped me clear many obstacles in my research.

And I would like to thank Dr Howe Tet Sen, our collaborator from Singapore General Hospital. He gave us lots of advice on the direction of the research. Moreover, all our samples are from him.

I also would like to thank all my fellow students and labmates. The discussion and sharing of knowledge among us helped me a lot in my research work. I want to thank all my friends for their support.

This research work is sponsored by National Medical Research Council. I would like to thank NMRC for their funding and support.

Publications

Ying Chen, Xianhe Ee, Wee Kheng Leow, Tet Sen Howe. Automatic Extraction of Femur Contours from Hip X-ray Images. In *Proceedings of First International Workshop on Computer Vision for Biomedical Image Applications* (CVBIA 2005) (in conjunction with International Conference on Computer Vision, 2005). Y. Liu, T. Jiang, C. Zhang (Eds.), LNCS 3765, Springer, 2005, pp. 200–209.

Vineta Lai Fun Lum, Wee Kheng Leow, Ying Chen, Tet Sen Howe, and Meng Ai Png. Combining Classifiers for Bone Fracture Detection in X-Ray Images. In *Proceedings of International Conference on Image Processing*, 2005.

Sher Ee Lim, Yage Xing, Ying Chen, Wee Kheng Leow, Tet Sen Howe, and Meng Ai Png. Detection of Femur and Radius Fractures in X-Ray Images. In *Proceedings of 2nd International Conference on Advances in Medical Signal and Information Processing*, 2004, pp. 249–256.

Dennis Wen-Hsiang Yap, Ying Chen, Wee Kheng Leow, Tet Sen Howe, and Meng Ai Png. Detecting Femur Fractures by Texture Analysis of Trabeculae. In *Proceedings of International Conference on Pattern Recognition*, 2004, volume 3, pp.

730–733.

Tai Peng Tian, Ying Chen, Wee Kheng Leow, Wynne Hsu, Tet Sen Howe, and Meng Ai Png. Computing neck-shaft angle of femur for x-ray fracture detection. In *Proceedings of International Conference on Computer Analysis of Images and Patterns*, 2003, LNCS 2756, pp. 82–89.

Contents

List of Figures

Summary

Extraction of bone contours from x-ray images is an important first step in computer analysis of medical images. It is more complex than the segmentation of CT and MR images because the regions delineated by bone contours are highly nonuniform in intensity and texture. Classical segmentation algorithms based on homogeneity criteria are not applicable. This thesis presents a model-based approach for either semi-automatically or automatically extracting femur contours from hip x-ray images. The semi-automatic method emphasizes reliability and accuracy. It requires users to manually align the model femur to the femur contour in the image. Then active contour is applied to accurately identify the femur contour. The automatic method emphasizes automation without user initialization. It works by first detecting prominent features. Then the model femur is registered to the x-ray image according to these features. Finally, the model is refined using active contour algorithm to get the accurate result. Experiments show that the semi-automatic method can always accurately extract the femur contours and the automatic method can extract the contours of the femurs with regular shapes, despite variations in size, shape and orientation.

Chapter 1

Introduction

1.1 Motivation

Imaging techniques are widely used in medical practice. It has become an important tool in many areas, such as surgery planning and simulation, intra-operative navigation, radiotherapy planning, and tracking of the progress of diseases, etc. As a result, a lot of research work has been done in computer-aided medical image analysis. For example, in the area of image-guided nero-intervention, MR images are analyzed to plan treatments of brain aneurysms and image-guided delivery of coils to the aneurysm. In the area of cancer imaging, x-ray, MR, and ultrasound images are analyzed to provide early detection, monitoring and treatment assessment of cancer. In the area of cardiac imaging, MR and ultrasound images are analyzed to get the time-varying information for tissue perfusion assessment. In such computer-aided analysis, the objects of interest must be isolated from the images. So segmentation and contour extraction of the objects of interest is the first step in these applications.

Our project team is working with Singapore General Hospital to develop x-ray image analysis systems. One of the system is for automated screening and detection of femur fractures. This system can help young doctors working in Emergency department to detect subtle fractures that they may miss due to inexperienced in reading x-ray images. It can also filter out those obviously healthy cases and alarm doctors to possible fractured cases. Methods of femur fracture detection with known contour have been developed [TCL+03, CYL+04, LXC+04]. Another system is for bone fracture surgery. For example, when a fracture occurred at the shaft part of a femur, there used to be some rotation between different broken parts of the femur. The surgeons must recover the original relative pose between different parts. Our system can help surgeons to estimate this relative pose by registering a 3D femur model to the bone contours in x-ray images. Both of these two systems require femur contours in x-ray images. So a method to extract femur contour is very useful and important.

But these two systems require different characteristics for the contour extraction method. For the surgery system, the extracted contour must be very accurate, otherwise the recovered 3D pose cannot be accurate. It is difficult to estimate what level of accuracy of the contour extraction method is enough for this surgery system, as it is expected that there will also be some errors from 3D registration and it is difficult to identify which error is from which part. So we hope the contour extraction method for the surgery system to be as accurate as possible. But generally, an error level of around 1 to 3 pixels is almost the limit of commonly used edge detection methods. More accurate edges can only be detected by applying sub-pixel edge detection. So it will be acceptable if the contour extraction method produces an error level of 1 to 3 pixels. However, this surgery system does not require the contour extraction method to be fully automatic because in one surgery, only one patient's x-ray image needs to be processed. It is possible to get some user input to help the contour extraction.

On the contrary, the contour extraction method for fracture detection must be fully automatic. Our screening system is expected to process a large batch of x-ray images from many different patients. It will be too tedious to let doctors give some input for each of these images. But the screening system does not require so accurate extraction results as the surgery system does. This is because the image features that are very near the contour normally do not give significant information about fractures. However, a reasonable contour is still necessary. If some loose bound, such as a bounding box, is used, too much noise from outside of the actual contour will be included for fracture detection, which will overwhelm the actual feature indicating fractures because this kind of features can be very subtle, as shown in Figure 1.1.

So we want to find two contour extraction methods. One method is semi-automatic and very accurate, which is for the surgery system. The other method is fully automatic but less accurate, which is for the screening system.

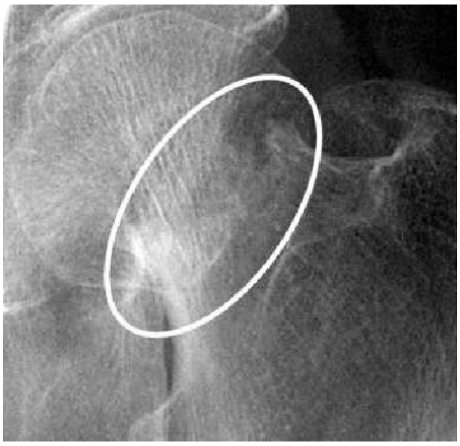

Figure 1.1: An example of subtle fracture.

1.2 Research Goal

The objective of this research is to extract the contours of the left femur and the right femur from a hip x-ray image. An example of the standard hip x-ray image is shown in Figure 1.2. The position, size and orientation of the femurs in all the input images are similar but not exactly the same. The ideal result will be a curve, consisting of a series of points, which coincides with the contour of the femur. An example of the desired result is shown in Figure 1.3.

In Figure 1.4, a typical example of the femur cropped from the hip x-ray image is shown. It can be seen that the image is generally very noisy. A lot of edges caused by the muscles or other bones can easily mislead the contour extraction algorithm. For example, the femoral head overlaps the pelvic bone, which makes it very difficult to get a clear contour of the head. The edge caused by the abdominal muscle, which usually passes the femur, and the muscles around the shaft can also mislead the algorithm. These extraneous edges and noise make fully automatic

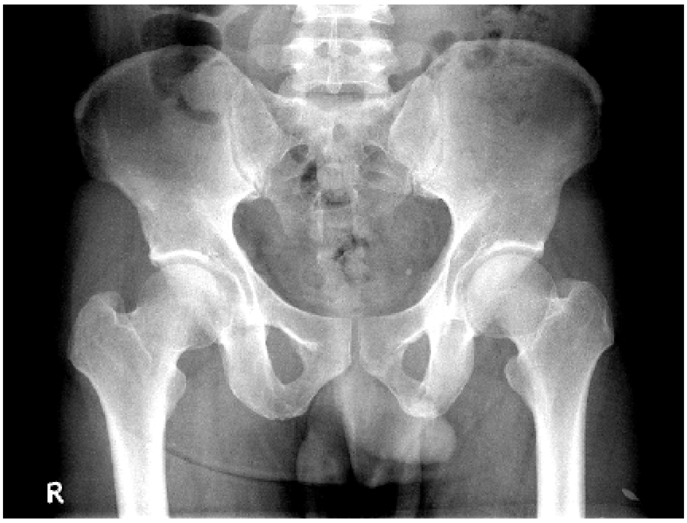

Figure 1.2: An example of the hip x-ray image.

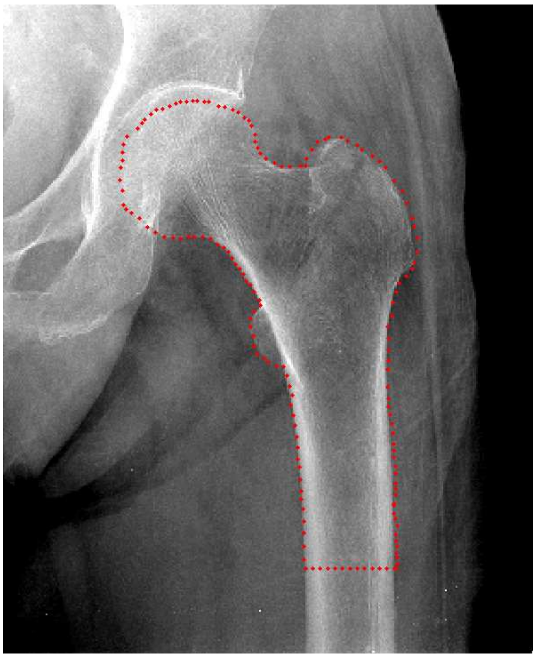

Figure 1.3: An example of the extracted femur contour.

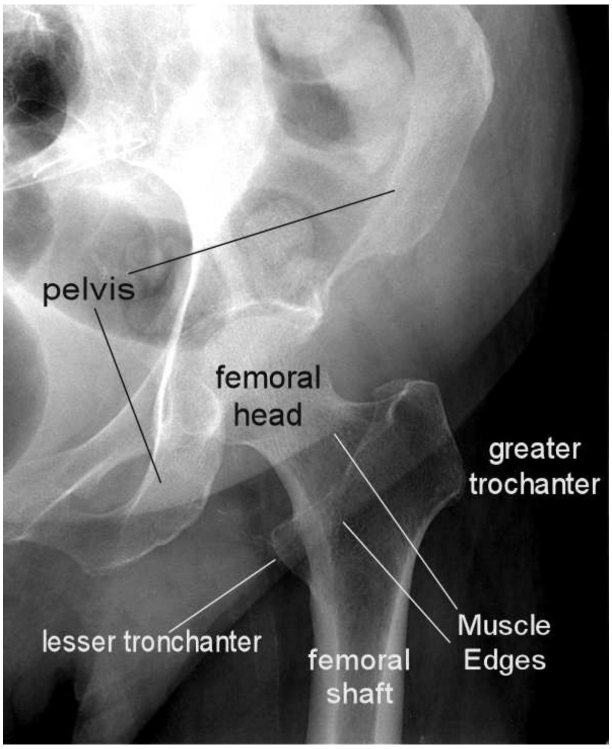

Figure 1.4: A typical femur x-ray image.

contour extraction very difficult.

A common way to avoid the noise is to initialize the model contour very near to the true contour. In existing x-ray image analysis applications, there are generally two initialization approaches. The first approach is manual initialization, which requires the user to input the initial contour. For example, in [LZYZ04], the system requires the user to provide the rough initial position of the target carpal bone, which is then deformed to get the true contour of the carpal bone, as shown in Figure 1.5. Generally, user input can make the problem easier to solve. But it makes the system not fully automatic.

Another approach is to automatically find the initial contour by some heuristic conditions. Normally, these heuristic conditions are obtained from prior knowledge of the target object, which is different for different object. For example, in [CJ04], the system tries to detect the gap between neighboring teeth and the gum line to form the initial contour of the tooth, as shown in Figure 1.6. In this way, the system can be fully automatic, but the accuracy of the result will highly depend on the detection result of the initial contour, which is affected by the target object and the input image. Moreover, the heuristic conditions make the system applicable only to specific body parts.

In general, fully automatic contour extraction of target objects with complex shapes from noisy images is a very difficult problem. In the system presented in this thesis, both approaches are implemented. The manual initialization approach can be used in situations where reliability and accuracy are very important and automation is not crucial. The automatic initialization approach can be used where the process must be automatic and a small amount of error can be tolerated.

1.3 Thesis Overview

The general outline of this thesis is as follows: Chapter 2 will introduce some related work. Chapter 3 will discuss the method of femur contour extraction with some minimal manual initialization. Chapter 4 will discuss the method of fully automatic femur contour extraction. And finally, Chapter 5 will discuss future work and Chapter 6 will conclude this thesis.

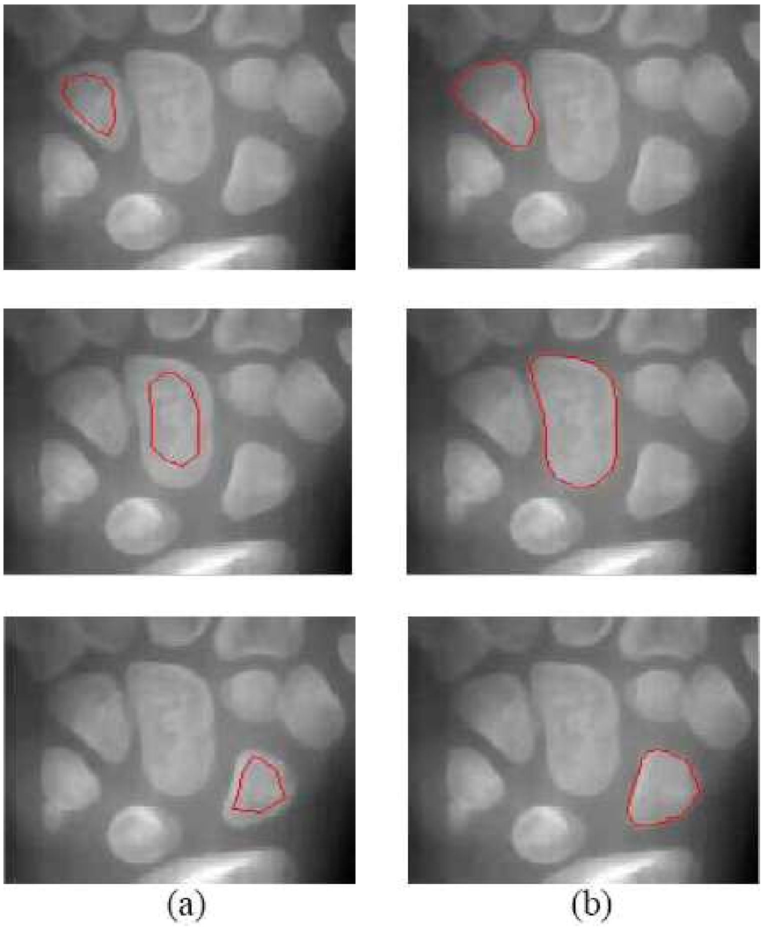

Figure 1.5: Carpal bone segmentation. (a) initial contour (b) final result (Figure 4 from [LZYZ04]).

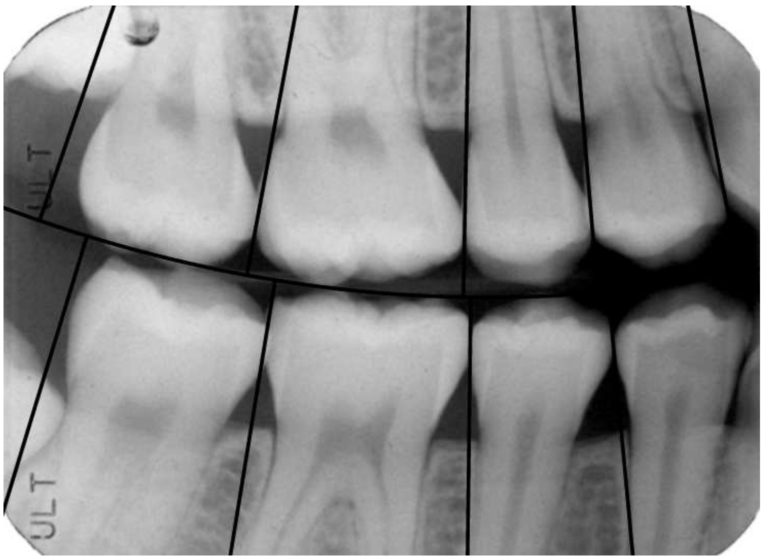

Figure 1.6: Tooth contour initialization (Figure 4 from [CJ04]).

Chapter 2

Related Work

Existing object contour extraction methods for medical images can be categorized into four general categories: segmentation, contour following, deformable models and atlas-based. These approaches are discussed in more details in the following sections.

2.1 Classical Segmentation Approach

Image segmentation and contour extraction are related in the sense that if an object is segmented from the image, then the contour of the object is available, and vice versa. But there are still some differences between segmentation and contour extraction under certain conditions. For example, classical image segmentation algorithms assume that the regions to be segmented contain homogeneous features so they attempt to segment an input image into regions based on feature homogeneity criteria. But contour extraction algorithms attempt to extract the contours of complete objects. If the target objects contain several regions with different features, the results of image segmentation and contour extraction will be different.

Image segmentation has been studied from a wide variety of perspectives. Lots of techniques have been proposed, including edge detection [Can86, Per80, Pra80], thresholding [LHKU98, LKC+95, SSW88], region growing and splitting [AB94, BJ88, DMS99, HS85], clustering [Cel90, Sch93, PB00, PHB99], watershed [GMA+04, RM00, Ser82], and classification [MFTM01, RM03, KGKW98, WGKJ96] etc. These methods have been applied for segmenting medical images into regions with homogeneous features such as brain [GDP+98, LHKU98] and tumor [GBBH96, PPO+96, LKC+95] in MR [BHC93, KGKW98] or CT [LS92] images.

However, these classical segmentation algorithms are not applicable to the extraction of femur contours in x-ray images because the homogeneity criteria are not satisfied for femurs in x-ray images. For instance, in a femur x-ray image, the femoral head region contains nonuniform texture pattern due to the trabeculae (Figure 2.1), and the femoral shaft region has nonuniform intensity due to the hollow interior within solid bony walls (Figure 1.4). Moreover, the femoral head overlaps with the pelvis bone (Figure 1.4). In this case, the extraction of femur contours becomes a more complex problem than classical image segmentation problem.

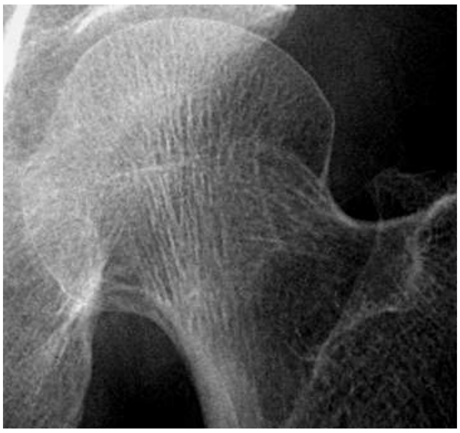

Figure 2.1: Close-up view of femoral head.

2.2 Contour Following Approach

Contour following is the most direct and intuitive approach, which is widely used in many applications [LNOK01, ZTMR01, LNY00, BC99, CHV$^+$97]. The basic idea is to select corners and local edge maxima as starting points, and then to follow a contour to another corner or local edge maximum by selecting the strongest edge in the following process. For example, Lourens et al. used this approach to extract contours from color images [LNOK01]. First of all, the image contrast is enhanced, and then the edge and corner points are detected. After that, a greedy contour following process is started from the edge and corner points. At the corner points, more than one contour can be followed. In the contour following process, a contour is always passing through the local gradient maximum. But in this approach, the contour following process can be easily misled by undesired edges. As discussed in the previous chapter, the femur x-ray images are very noisy. It is very difficult to control the contour following algorithm to always pick the right edges.

2.3 Deformable Model Approach

Deformable model approach is to let the model of the target object deform under certain constraints and finally snap onto the contour of the target object. Some commonly used methods in this approach include active contour, active shape and level set method.

2.3.1 Active Contour

Active contour [KWT88, TPBF87, TWK88], or snake, method deforms the initial contour by minimizing the total energy of the contour. Three kinds of energy terms can be defined in active contour:

1. Internal energy, which constrains the stretching and bending of the contour.
2. Image force, which is the image feature such as image intensity or edges attracting the contour.
3. External force, which constrains the deformation of the contour.

The external force can be absent, and then the deformation of the model is only affected by the image features, which makes the model very sensitive to noise and its initial configuration. An example of extraction of carpal bone contours using active contour is shown in Figure 1.5.

A lot of improvements to the snake have been proposed. For example, Xu et al. suggested using gradient vector flow (GVF) as the image force to make the snake less sensitive to its initial configuration and capable of snapping to concave object boundaries [XP97]. Some other methods incorporate geometric constraints in the snake. For example, Shen et al. [SHD01] embedded geometric information as attribute vector into the snake. The attribute vector contains the areas of triangles formed by each point on the snake and their two neighboring points. During the snake's evolution process, the areas of the triangles are constrained. Foulonneau et al. [FCH03] includes Legendre moments in the snake to provide global description of a reference shape.

Active contour method has been used for segmentation of brain in MR images [AM00], liver [GKK98, YF03] or heart [SHC94] in CT images, and blood vessels [XSK+94] in HVEM images. In general, the active contour method is still very sensitive to noise and requires good initialization. And snake cannot handle topology change.

2.3.2 Active Shape

Basically, active shape model (ASM) [CHTH94] is a statistical model generated from a set of training samples. A series of corresponding points, called landmark points, are identified on the boundary of the target object in each training image. Then the training samples are regarded as vectors and statistical parameters of the vector distributions are computed using principal component analysis. By changing the parameters, new shapes can be synthesized.

The contour extraction process using ASM is actually a process of synthesizing an optimal shape that is most similar to the shape in the image. The statistical difference between the synthesized shape and the original model can be calculated. By restricting the difference to small values, the deformation can be limited to

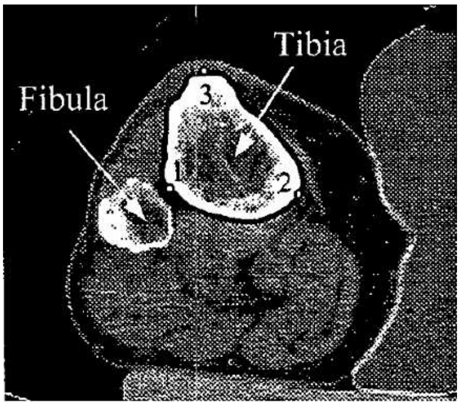

Figure 2.2: Extraction of tibia contour using ASM. The labelled points 1, 2, 3 are landmarks

an acceptable range. An example of extraction of tibia contour from ultrasound images using ASM is shown in Figure 2.2.

ASM has been applied for segmentation of tibia bone in ultrasound images [HZ01], heart in echocardiographic images [HG00] or MR images [OBHF03], and vertebra in CT images [STA96]. ASM is more suitable for the situation where the shape of the target object can be controlled by not too many parameters. Otherwise it will be too difficult to synthesize the optimal shape. Moreover, many training samples are needed to correctly compute compute the statistical distribution.

2.3.3 Level Set

The level set method is proposed by Sethian et al. [Set96]. The idea of this method is to handle the topology change problem in one higher dimension. Let Γ denote a closed 2D curve. To deform Γ, a 3D function $\phi(x, y, t)$ is defined. This is called

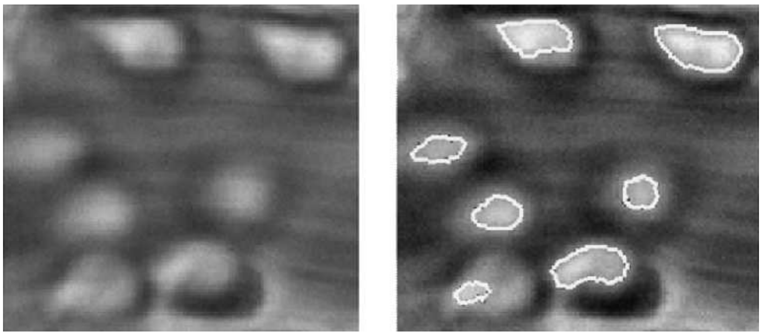

Figure 2.3: Extraction of leukocyte using level set.

the level set function. The solution of $\phi(x, y, t = 0) = 0$ is the initial contour. This is called the zero level set. Deformation of Γ is achieved by moving the level set function ϕ along the time axis t. Then, solution of $\phi = 0$ at time t is the desired contour. Let F denote the force that gives the speed of Γ in its normal direction. Then, the change of ϕ over time t, ϕ_t, is given by the equations:

$$\phi_t + F|\nabla\phi| = 0, \tag{2.1}$$

$$\phi(x, y, t = 0) = \Gamma. \tag{2.2}$$

An example of extraction of leukocyte contours using level set methods is shown in Figure 2.3. As level set method can easily handle topological changes, multiple leukocytes can be extracted with a single initial contour.

The level set method has been applied for brain segmentation in MR images [Sur01, MA98], detection and track of leukocyte [MRA04] and extraction of pulmonary vessels [ZBJ$^+$98] from CT images. The level set method can easily handle topological changes of the contour. But it generally does not preserve the shape information.

2.3.4 Summary

These deformable approaches are contour-based instead of region-based. So unlike the classical segmentation methods, they have the potential of extracting contours of body parts that do not contain homogeneous features. An important weakness of these approaches is that they are typically sensitive to noise. So they usually require good initialization to produce good results. Otherwise, these methods can be easily affected by noise and extraneous edges in the image, resulting in incorrect extraction of object contours.

2.4 Atlas-Based Approach

The atlas-based approach [PXP00] can solve the initialization problem of deformable model approach. This approach first constructs a spatial map called atlas based on some prior knowledge. The prior knowledge can be the contour of the surface of target objects, the spatial relationship between different objects in input images, etc. The atlas can be constructed from a single sample. It can also be constructed by finding the spatial distribution of objects from a set of training samples, resulting in probabilistic atlas.

After construction, the atlas is aligned to the input image by some global transformation. Then, local deformation of each part of the atlas is performed to accurately extract the contours of the target objects. Local deformation can be achieved using deformable model methods described in Section 2.3 or other free-form deformable methods.

Atlas approach has been applied for segmentation of brain CT images [AOB03], brain MR images [ANWD99, SHD01] and abdominal CT images [PBM03]. Atlas-based approach is typically application specific. Different objects or input images normally contain different prior knowledge. So different atlas must be used. And in our application, the atlas-based approach can still face difficulties because the femurs in different images can be oriented differently due to variations in the patients' standing postures resulting from femur fractures. Incorporating articulation of body parts in the atlas-based approach may help to solve the problem of model initialization but it makes the atlas very complex and difficult to use.

Chapter 3

Contour Extraction with Minimal User Input

3.1 Overview

This chapter will describe the method for contour extraction with some user inputs. As discussed in Section 1.2, fully automatic contour extraction of the femur bone from noisy images is very difficult. And under certain situations, the reliability and accuracy of the extraction algorithm is very important while its automation is not so crucial. Then this semi-automatic method can be used. For example, in the operation theater, the surgeons need to estimate the relative pose of the broken parts of the femur bone. One way is to register the 3D femur model to the bone contours in the fluoroscopic x-ray images (Figure 3.1). To do this, the contour must be as accurately extracted as possible. But whether the method is automatic is not so important as the target is just one image, not a batch of

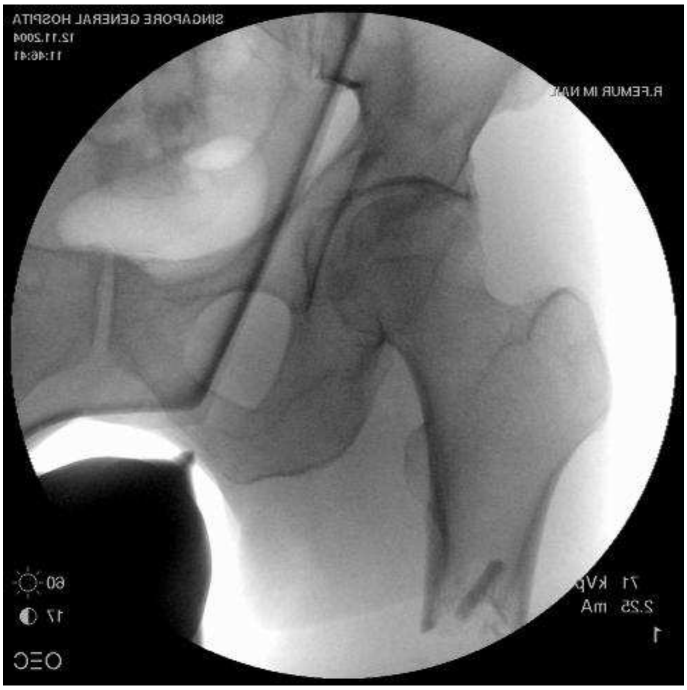

Figure 3.1: An example fluoroscopic x-ray image.

many images.

The overview of this system is shown in Figure 3.2. First of all, a model femur contour is manually aligned with the femur contour in the image. Then the active contour algorithm is applied to refine the aligned femur contour to accurately identify the femur contour in the image.

3.2 Manual Alignment

As discussed in Section 1.2, a good initialization is very important to get an accurate result. And user input is always a reliable source of initialization. But some guidelines are still essential to help a user generate a good initialization and to reduce the amount of work required from the user. So a simple GUI with an

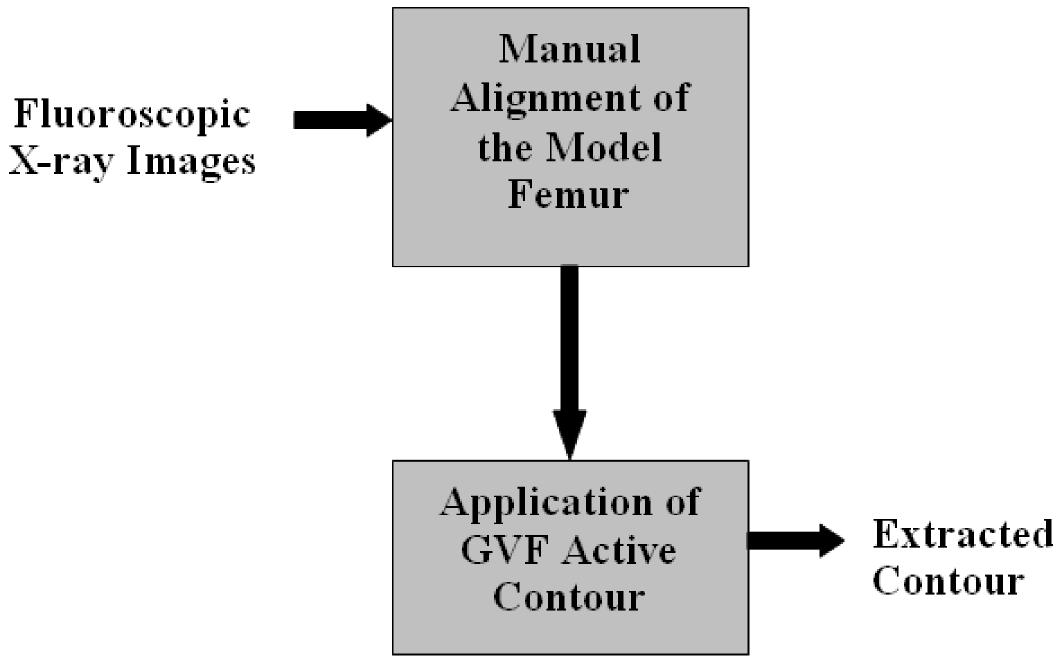

Figure 3.2: Overview of femur contour extraction with user inputs.

existing femur model is developed. The user can control some key features of the femur shape and intuitively see how to deform the shape to produce a good initialization. The user can easily drag, scale and rotate the model.

Basically, the whole process is divided into five steps. In the first step, the user moves and scales the whole model to align with femoral head (Figure 3.3). The femoral head is chosen as the first femur part to be aligned because it is circularly symmetric. So, only translation and scaling are required.

In each of the next four steps, a segment of the model femur contour is deformed and aligned to the femur contour in the image (Figure 3.4–3.7). Each segment is defined by two fixed end points $\mathbf{u}_1$ and $\mathbf{u}_2$ and a movable feature point $\mathbf{v}$ located between $\mathbf{u}_1$ and $\mathbf{u}_2$. As $\mathbf{v}$ is moved to a new position $\mathbf{v}'$, the segment undergoes a similarity transformation, which includes scaling and rotation. The subsegment from $\mathbf{u}_i, i = 1, 2$, to $\mathbf{v}'$ is rotated about $\mathbf{u}_i$. So, the scaling factor s_i is given by

$$s_i = \frac{\|\mathbf{v}' - \mathbf{u}_i\|}{\|\mathbf{v} - \mathbf{u}_i\|} \tag{3.1}$$

and the rotation matrix $\mathbf{R}_i$ can be obtained by solving the equation

$$\mathbf{v}' - \mathbf{u}_i = s_i \mathbf{R}_i (\mathbf{v} - \mathbf{u}_i). \tag{3.2}$$

Then any point $\mathbf{p}$ lying on the subsegment from $\mathbf{u}_i$ to $\mathbf{v}$ is moved to the new point $\mathbf{p}'$ given by

$$\mathbf{p}' = s_i \mathbf{R}_i (\mathbf{p} - \mathbf{u}_i) + \mathbf{u}_i. \tag{3.3}$$

Sample results of these four steps are shown in Figure 3.4–3.7. In these figures, the green dots are the fixed end points and the black dots are the movable feature points. In the second step (Figure 3.4), the upper corner point of the greater trochanter is the movable feature point. The contour from the joint between femoral head and the upper boundary of the neck to the bottom of the right boundary of the shaft is adjusted accordingly. In the third step (Figure 3.5), the lower corner point of the greater trochanter is the movable feature point. The contour from the upper corner of the greater trochanter to the bottom of the right boundary of the shaft is adjusted accordingly. In the fourth step (Figure 3.6), the midpoints of the line segment connecting the bottoms of the two boundaries of the shaft is the movable feature point. The contour from the lower corner of the greater trochanter to the joint between the femoral head and the lower boundary of the neck is adjusted accordingly. In the fifth step (Figure 3.7), the midpoint of the lesser trochanter is the movable feature point. The contour from the bottom

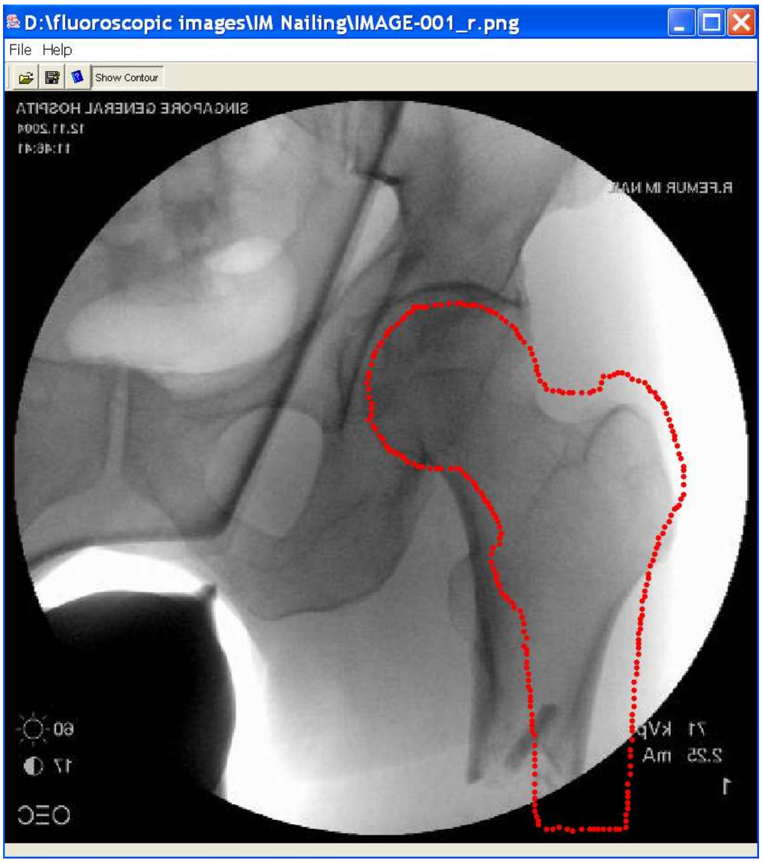

Figure 3.3: Manual alignment: Step 1. This step involves global translation and scaling of the whole model to fit the femoral head part.

of the left boundary of the shaft to the joint between the femoral head and the lower boundary of the neck is adjusted accordingly.

The segments adjusted in two consecutive steps overlap each other. The reason for this design is that each part of the femur contour normally is affected by two feature points. And the overlapping parts are adjusted in the process of moving the two corresponding feature points. The model femur contour is aligned better in this way.

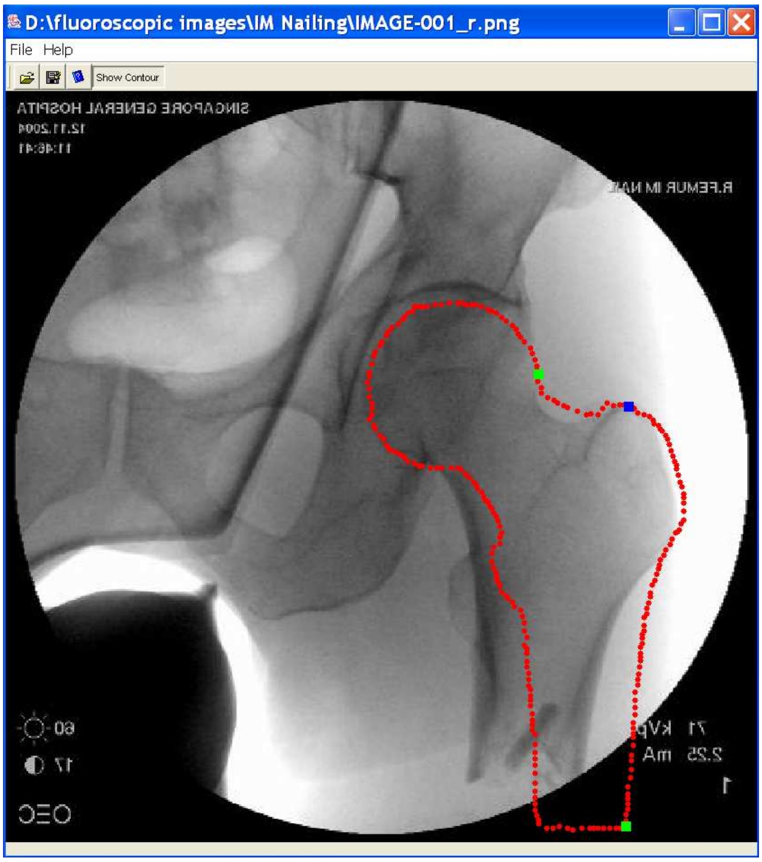

Figure 3.4: Manual alignment: Step 2. This step adjusts the model to fit the upper corner point of the greater trochanter. The green dots are the fixed end points and the black dot is the movable feature point.

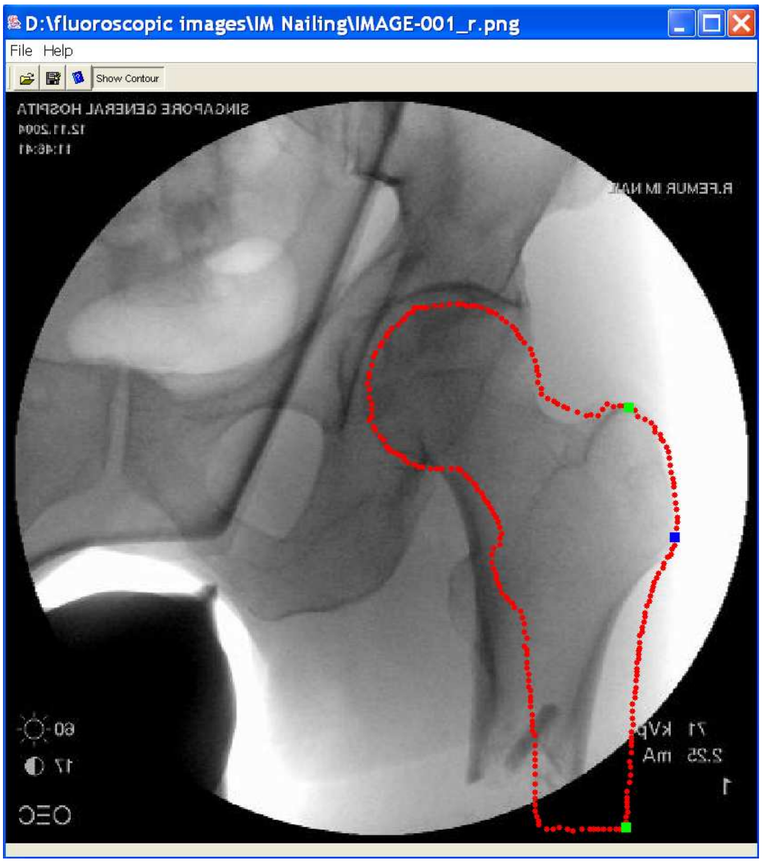

Figure 3.5: Manual alignment: Step 3. This step adjusts the model to fit the lower corner point of the great trochanter.

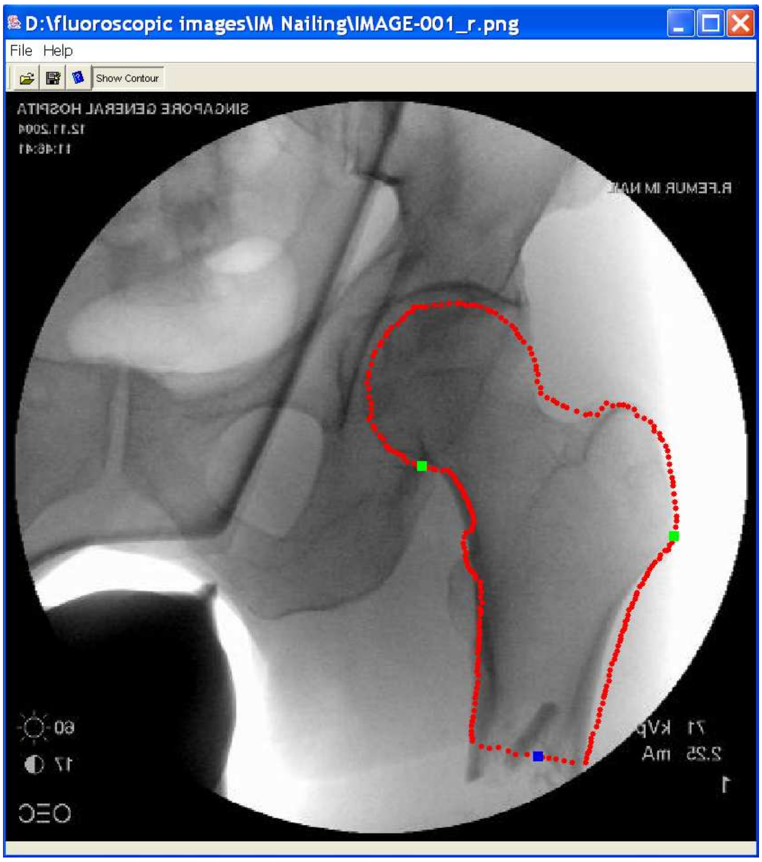

Figure 3.6: Manual alignment: Step 4. This step fixes the orientation and width of the shaft.

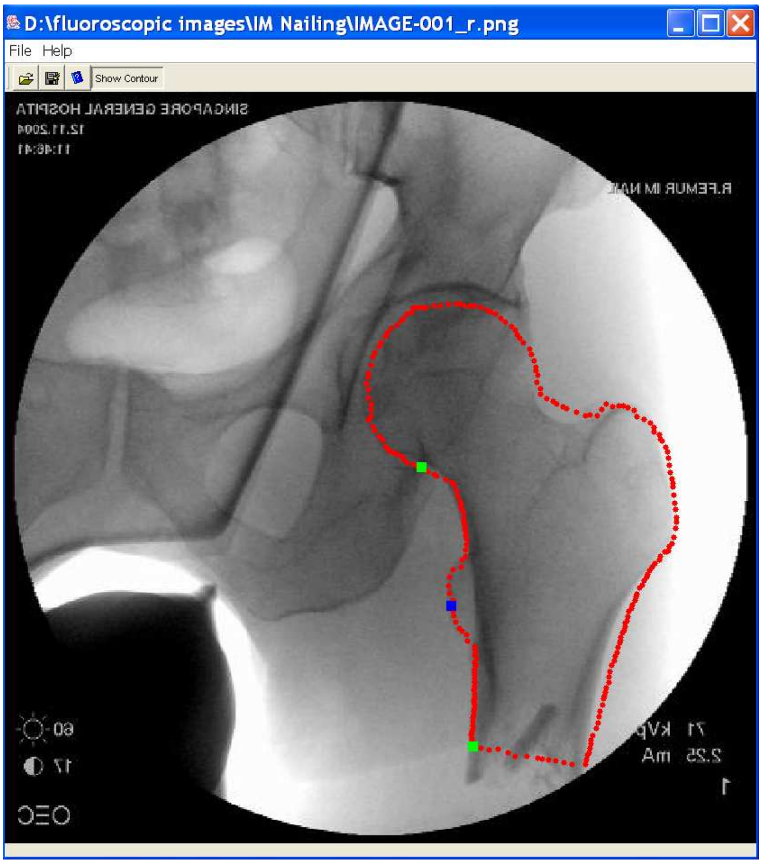

Figure 3.7: Manual alignment: Step 5. This step fixes the position and size of the lesser trochanter.

3.3 Active Contour

The aligned femur model from the previous step is used as the initial configuration of the active contour. And edges of the image are detected. From the edges, the gradient vector flow (GVF) field is computed. Then it is used as the external energy to attract the active contour to the correct femur contour.

3.3.1 Edge Detection

A modified Canny edge detector is applied here, which is proposed by Tian [Tia02]. The original Canny edge detector [Can86] works on gray scale images to find the edges. It first smoothes the image using a Gaussian filter. Then it applies a 2D first derivative filter on the smoothed image to calculate the gradient magnitude and orientation. Next, it suppress those non-maximal pixels along the gradient direction to find the local peaks. And finally, it links up the edges using double thresholding.

But if Canny edge detector is directly applied on the femur images, it will either produce too much noise, if a lower threshold is used, or lose some actual edges at the femoral head (Figure 3.8). So Tian et al. proposed a modified Canny edge detector to solve the problem [Tia02]. The idea is to preserve the edges at the femoral head and remove the noise at the same time by looking at the pixel intensity. Observation shows that the pixels on the bone region normally have higher intensity values than the noise. So the modified Canny edge detector first detects all edges using small smoothing effect and low threshold value, then suppress those edge points with low intensity values, which is very likely to be

(a) (b) (c)

Figure 3.8: Result of Canny edge detection. (a) Original femur images. (b) Canny edges with low threshold values. (c) Canny edges with more smoothing and higher threshold values (Figure 3.2 in [Tia02]).

noise. The result of the modified Canny edge detector is shown in Figure 3.9. The percentage values determine the thresholds. For example, 20% means the threshold is larger than the gradient magnitude of 20% of all the pixels. An example of the edge detection result of fluoroscopic image is shown in Figure 3.10.

3.3.2 Active Contour and Gradient Vector Flow

Active contour, or snake, is applied in the method to refine the snake to better match the femur contour in the image. This method is proposed by Kass et al [KWT88], which is basically an energy minimization process. The total snake

(a) (b) (c) (d)

Figure 3.9: Modified Canny edge detection with various threshold values. (a) 20%, (b) 50%, (c) 70%, (d) 90% (Figure 3.3 in [Tia02]).

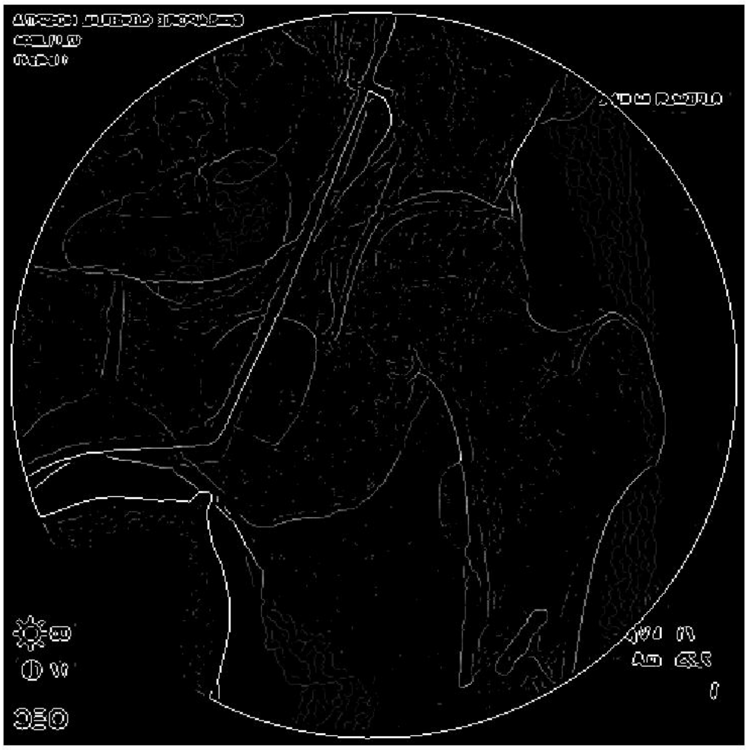

Figure 3.10: An example of edge detection result of a fluoroscopic image.

energy is defined as :

$$E_{snake} = \int_0^1 [E_{int}(\mathbf{v}(s)) + E_{image}(\mathbf{v}(s))]ds \tag{3.4}$$

where $\mathbf{v}(s)$ is the parametric curve representing the contour. E_{int} is the internal energy, which is the sum of a first-order term and a second-order term, defined as follows:

$$E_{int} = \frac{1}{2}[\alpha(s)\|\mathbf{v}_s(s)\|^2 + \beta(s)\|\mathbf{v}_{ss}(s)\|^2] \tag{3.5}$$

and $\mathbf{v}_s(s)$ and $\mathbf{v}_{ss}(s)$ are the first derivative and second derivative of $\mathbf{v}(s)$ respectively. The first-order term represents the elasticity of the contour while the second-order term represents rigidity. They are controlled by $\alpha(s)$ and $\beta(s)$. The larger the value of $\alpha(s)$ and $\beta(s)$, the more the contour shrinks.

E_{image} is the image feature which the snake is expected to snap to. In the case of contour extraction, it should be the edges. But the snake as defined above cannot snap well to the concave parts of the contour as shown in Figure 3.11. To overcome this shortcoming, gradient vector flow (GVF) is proposed by Xu et al. [XP97]. GVF field is a vector field $\mathbf{g}(x, y) = (u(x, y), v(x, y))$ that minimizes the energy functional

$$\mathcal{E} = \iint \mu(u_x^2 + u_y^2 + v_x^2 + v_y^2) + \|\nabla E\|^2\|\mathbf{g} - \nabla E\|^2 dx\, dy \tag{3.6}$$

where μ is a constant that is set according to the amount of noise present, and u_x, u_y, v_x, and v_y are the partial derivatives of u and v with respect to x and y. ∇E is the gradient vector normal to the edge E derived from the image. Using variational calculus, it can be shown that the GVF field can be computed by

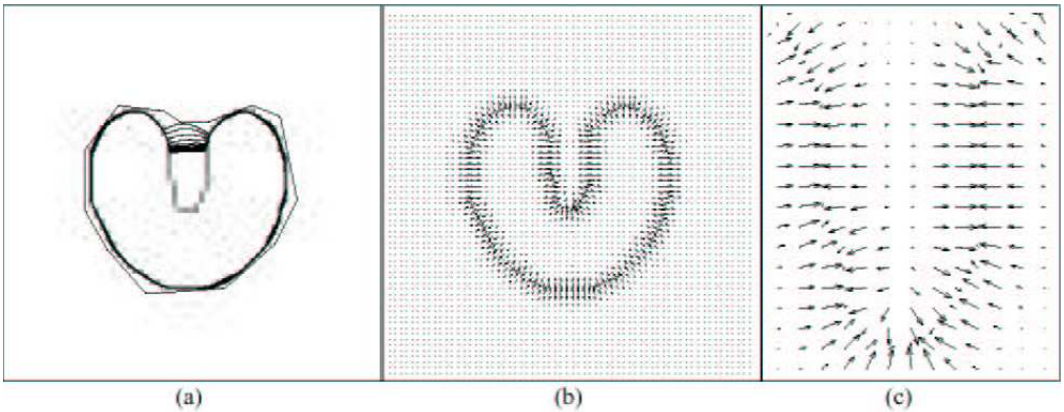

Figure 3.11: (a) Convergence of snake. (b) Traditional potential force. (c) Close-up at concavity: no force to attract the snake towards the bottom of the concavity (taken from [XP97]).

solving the following Euler equations:

$$\begin{aligned} \mu\nabla^2 u - (u - E_x)(E_x^2 + E_y^2) &= 0 \\ \mu\nabla^2 v - (v - E_y)(E_x^2 + E_y^2) &= 0 \end{aligned} \tag{3.7}$$

where E_x and E_y are the partial derivatives of E with respect to x and y.

Basically, GVF is derived from the diffusion of the gradient vectors of the edge map. The forces pointing to the concave edge will be diffused out so that the snake can be attracted to the edge, as shown in Figure 3.12. The small arrows stand for the direction of the image force. By comparing Figure 3.11 and Figure 3.12, it can be seen that in the traditional force field, there is no force at the top of the concavity to attract the snake to the bottom of the concavity. So the snake cannot converge to the bottom of the concavity. In the GVF field, there are such forces. Therefore, the snake can snap onto the desired contour with concave parts by minimizing the total energy E_{snake}.

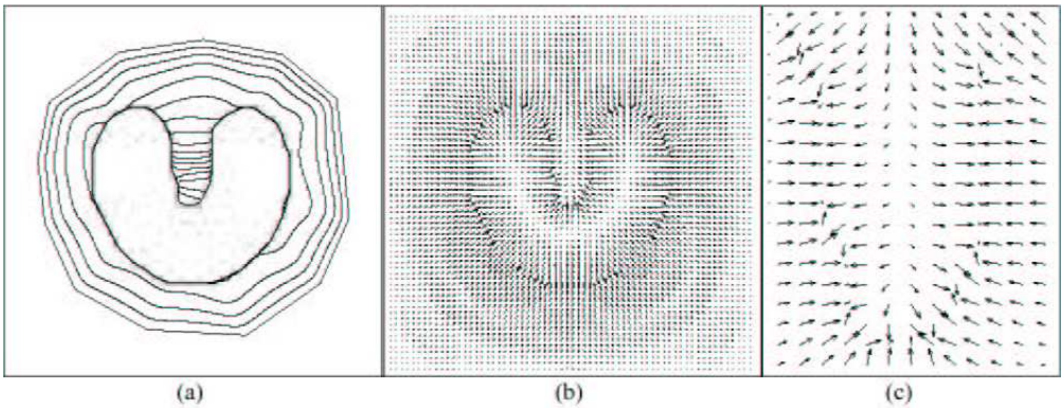

Figure 3.12: (a) Convergence of snake. (b) GVF external force. (c) Close-up at concavity: forces exist to attract the snake towards the bottom of the concavity (taken from [XP97]).

After manual initialization of the model femur contour described in Section 3.2, the GVF snake is applied to deform the model femur contour to align accurately with the target femur contour in the image. In current implementation, uniform α and β values are used. Since the snake is well initialized by manual alignment of the model femur contour, the snake can accurately snap onto the target femur contour. And the snake converges very fast.

3.4 Experiments and Discussion

A testing set of 4 fluoroscopic x-ray images and 30 normal femur images cropped from standard hip x-ray images were used to test the contour extraction method with manual model alignment. The size of fluoroscopic x-ray images was 490×490. The size of the normal femur images was 297×348. The error of an extracted contour is measured in terms of the mean error between the points on the extracted contour and their closest points on the manually marked contour, which is regarded as the ground truth.

The method successfully extracted the femur contours in all testing samples. For the fluoroscopic x-ray images, the mean and the standard derivation of the error are 0.239 pixel and 0.123 pixel (Figure 3.13). For the normal femur images, mean and the standard deviation of the error are 1.32 pixels and 0.30 pixel (Figure 3.14).

The method accurately extracted the femur contours in all testing images despite variations in size, shape and orientation. The errors of the extracted contours are very small. They are no more than 2.06 pixels, which are only 0.6% of the image size. This shows that the manual initialization approach is very reliable and accurate.

The accuracy of the results reply on the initialization and image nature. An example of different extraction results from the same image with different initialization is shown in Figure 3.15. It is shown that at some parts where there are many edges from other bones, e.g. femoral head (Figure 3.15(b)) and neck (Figure 3.15(c)), the contour can be easily distracted if the initialization is not close enough to the desired edges, while at those parts where the image is very clear, e.g. femoral shaft (Figure 3.15(d)), even if the initialization is quite far away from the desired edge, the contour can still snap onto the desired edge.

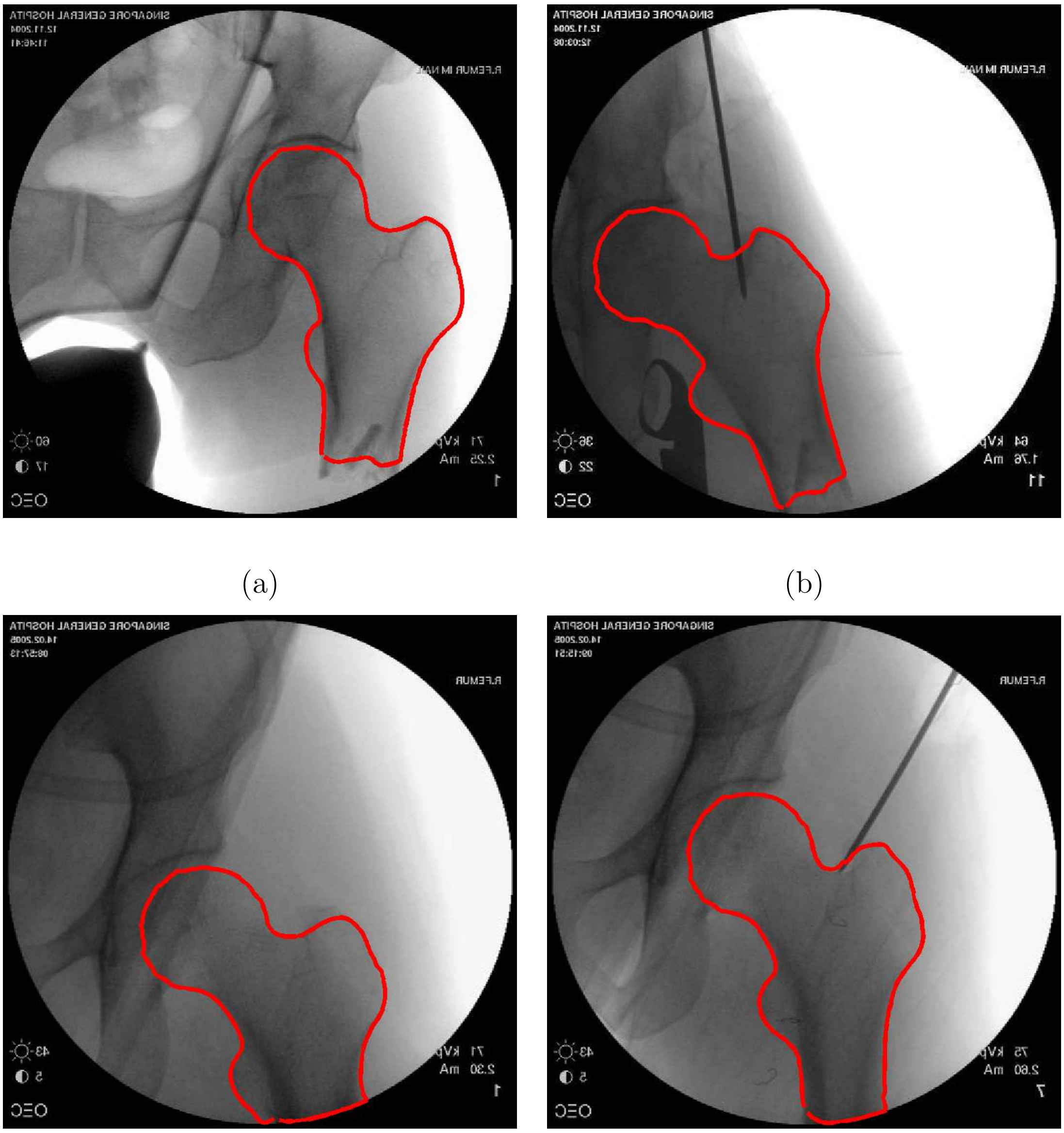

(a) (b)

(c) (d)

Figure 3.13: Test results of fluoroscopic x-ray images. The errors are (a) 0.299 pixel, (b) 0.150 pixel, (c) 0.126 pixel and (d) 0.384 pixel.

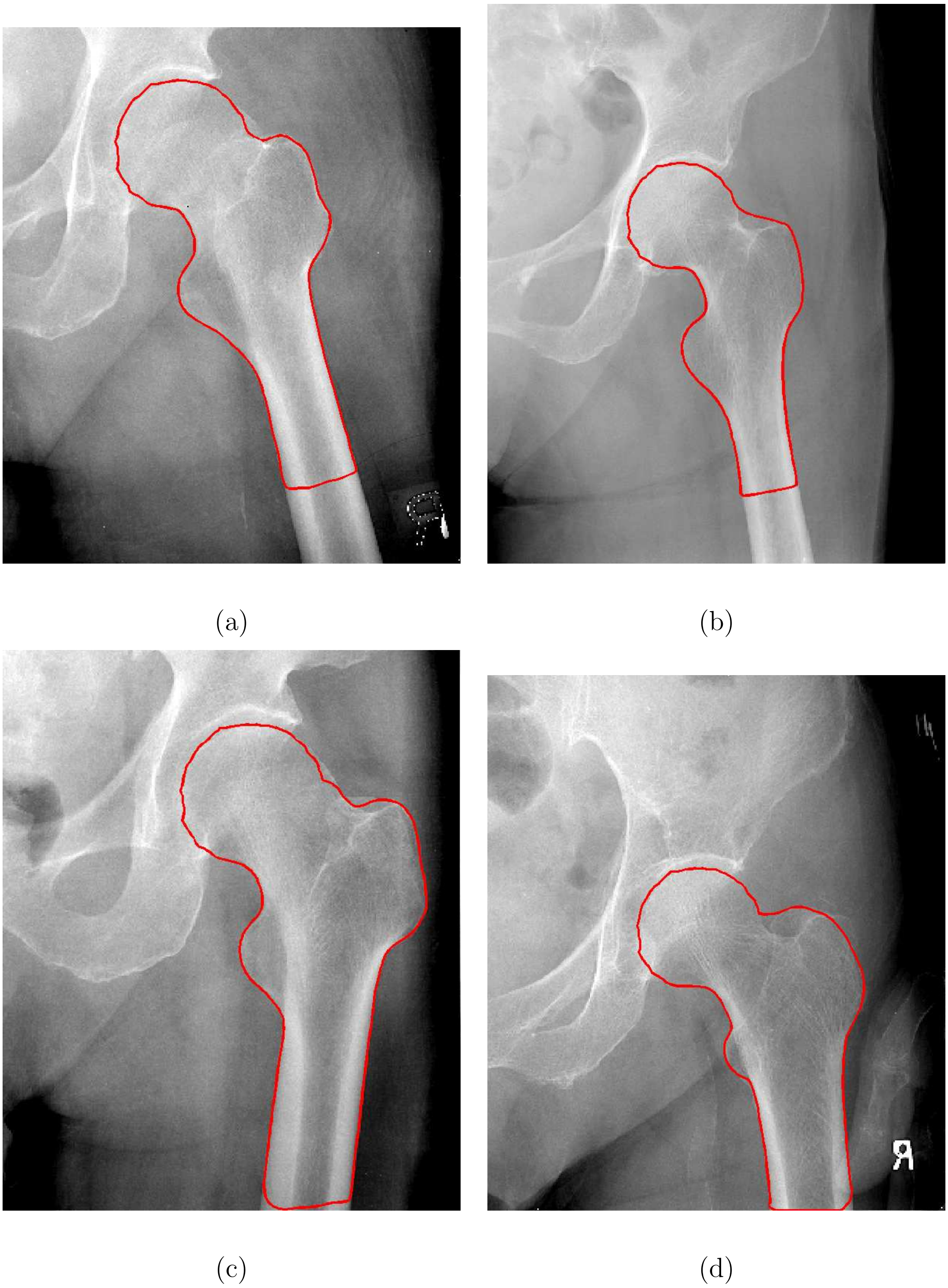

Figure 3.14: Test results of normal x-ray images. The errors are (a) 2.06 pixels, (b) 1.10 pixels, (c) 1.68 pixels and (d) 1.82 pixels.

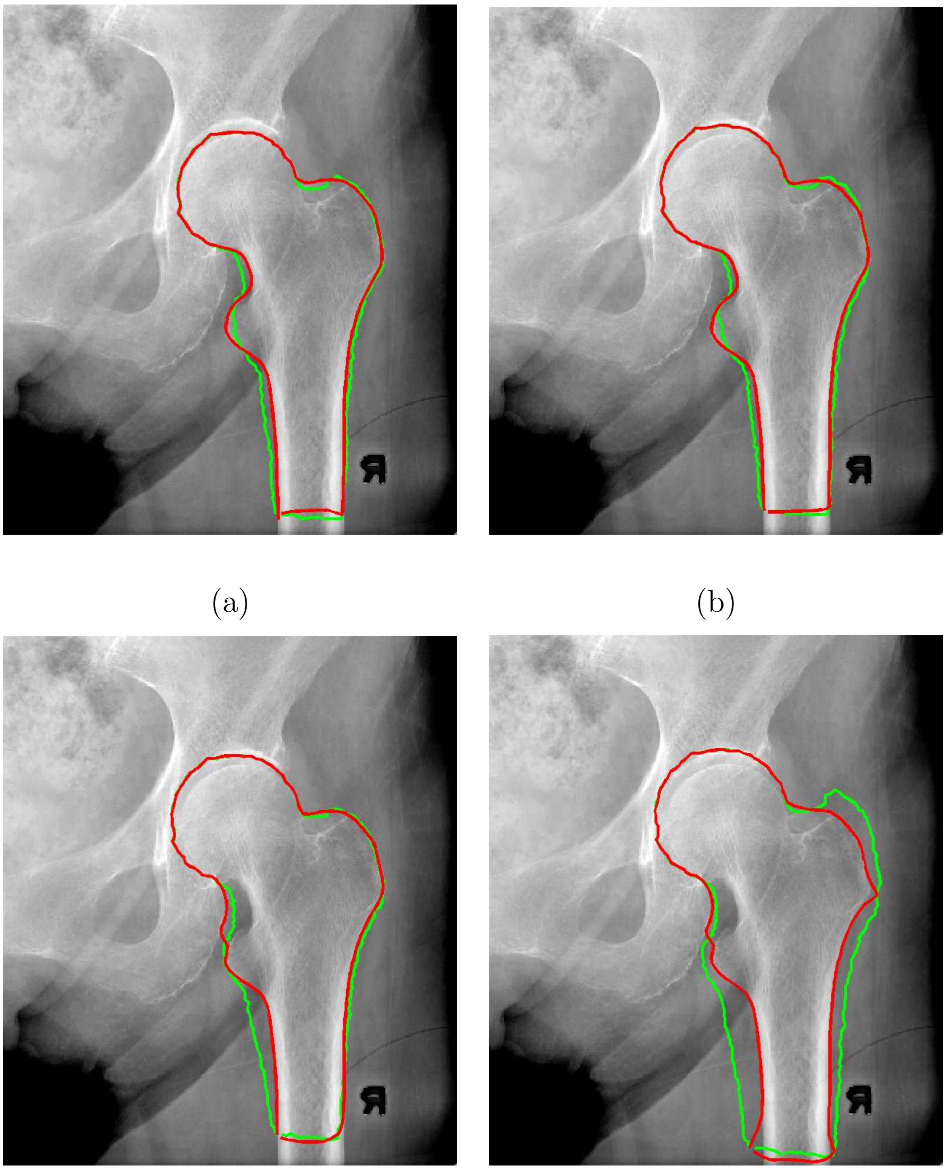

(a) (b)

(c) (d)

Figure 3.15: Sensitivity of snake initialization (green curves) on the extracted results (red curves). (a) An optimal result. (b–d) Results affected by extraneous edges in the image.

Chapter 4

Automatic Contour Extraction

4.1 Overview

As discussed in Section 3.1, semi-automatic contour extraction with minimal user inputs is suitable when reliability and accuracy are more important than automation. But in some applications, the situation is reversed. For example, when many x-ray images need to be screened, a fully automatic method is more efficient than a semi-automatic one. In current clinical practice, x-ray images are visually inspected by doctors. But this work is very tedious and when the doctors get tired, errors can happen. So some algorithms are developed to help the doctors to automatically screen the x-ray images [TCL+03, CYL+04, LXC+04]. In this case, automation is very crucial. The system cannot reduce the doctors' workload if it still requires users' inputs in segmenting each input image. However, a small amount of errors in contour extraction can be tolerated because the fracture detection algorithms work according to the image feature inside the femur contour.

The features that are very near to the femur contour do not affect the classification result significantly.

This chapter describes the fully automatic femur contour extraction method. The method takes a standard hip x-ray image (Figure 4.2) as the input. It consists of three main stages as shown in Figure 4.1.

1. Delineation of the regions that contain the left and the right femurs.

2. Registration of a 2D model femur contour to femur regions in the image.

3. Application of the active contour algorithm with shape constraints to refine the femur model to accurately identify the femur contour in the image.

4.2 Delineation of Femur Regions

This stage is straightforward because the pose of the patients are similar when the hip x-ray images are taken. The femurs always fall in the left and right bottom corners of the images. Based of 50 training samples, it is determined that the femur region falls within a bounding box of size 990×1160 pixels (Figure 4.2). The delineated regions are cropped out and used as inputs to the following stages. All the images of right femurs are reflected so that they can be analyzed using the same algorithm as for left femurs.

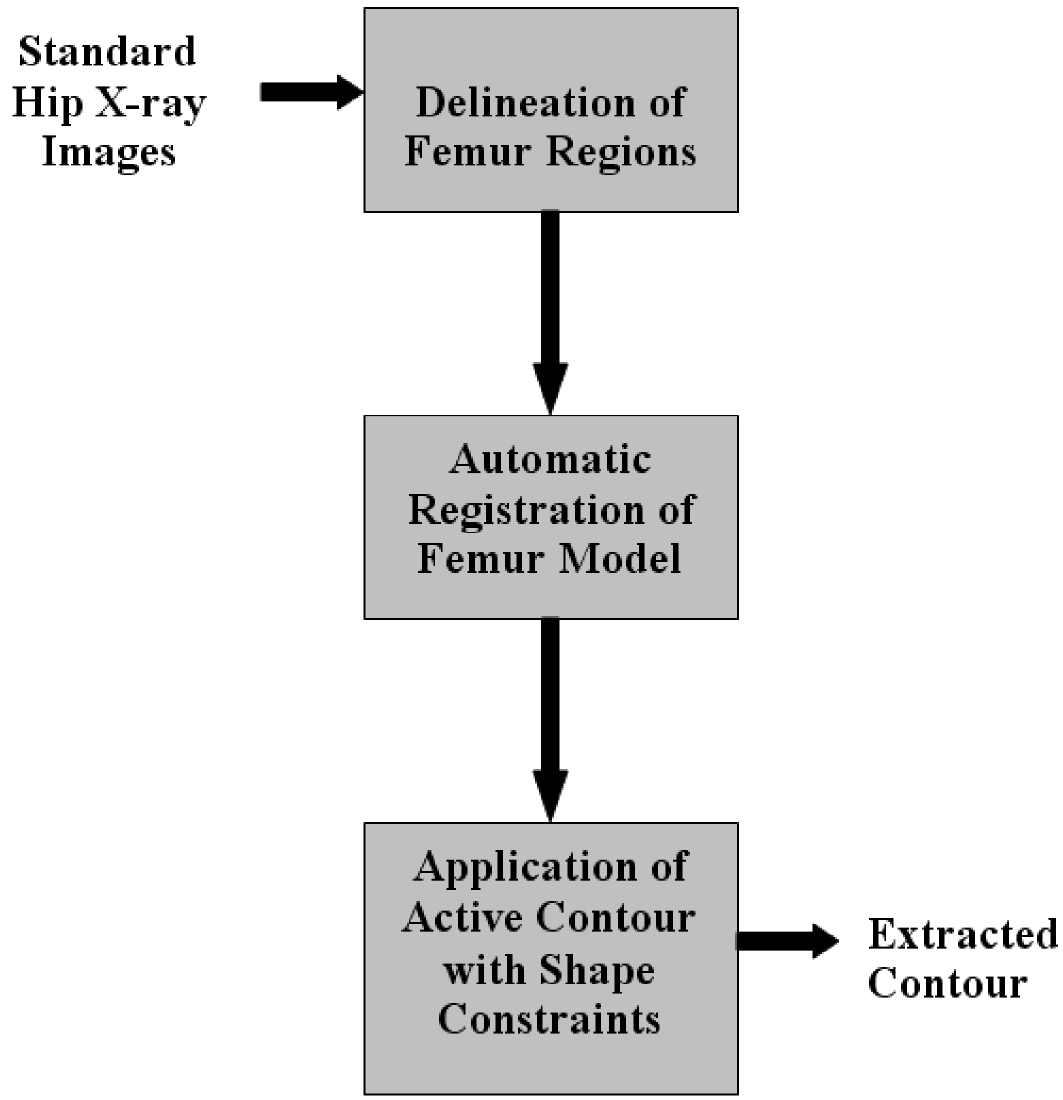

Figure 4.1: Overview of automatic femur contour extraction method.

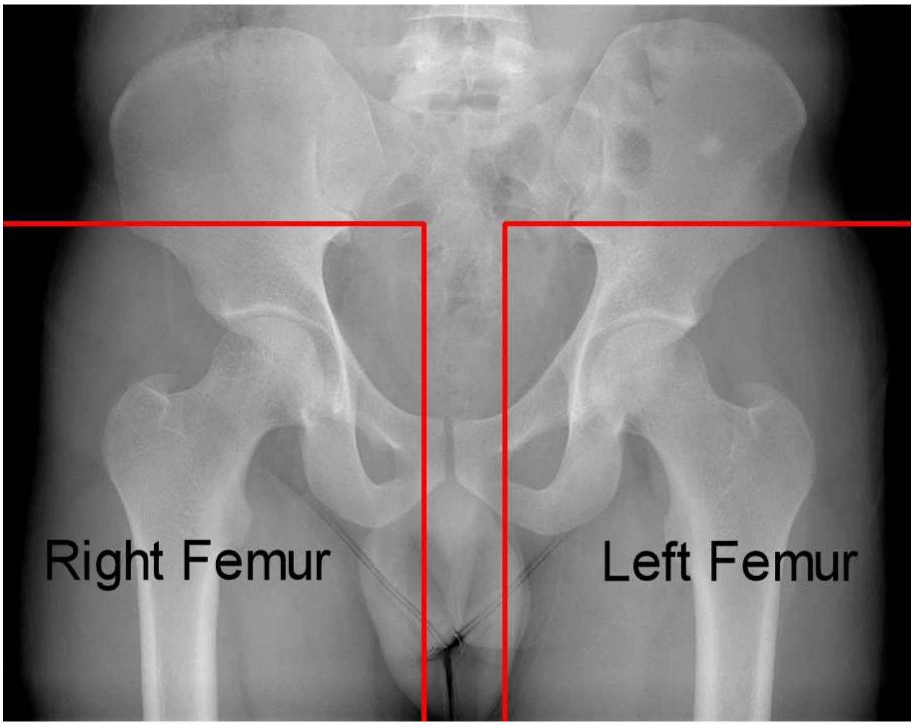

Figure 4.2: Cropping the left and right femurs from the hip x-ray image.

4.3 Registration of Femur Model

This stage applies prior knowledge about the femur to register a model of the femur contour to the one in the image. It consists of four main steps:

1. Detection of candidate femoral shafts represented by pairs of parallel lines.
2. Detection of candidate femoral heads represented by circles.
3. Detection of candidate turning points near the base of the greater trochanter.
4. Piecewise registration of model femur contour.

4.3.1 Detection of Candidate Femoral Shafts

The outer contours of the femoral shaft consists of two approximately parallel straight lines. These two lines always start from the bottom of the image. They are the most consistent features in all the images. So, the natural way to start is to detect femoral shaft by finding a pair of long parallel straight lines at the bottom of the image.

Femoral shaft detection is performed as follows. First, up to 8 points near the bottom of the image with the largest horizontal intensity gradient components are identified (Figure 4.3). These are good candidate feature points because the points on the shaft contours have very large intensity gradients. The directions of the intensity gradients at these points should not be larger than 30° because the shafts are roughly vertical in the images.

Next, contour following method is applied to identify approximately straight lines starting at the points detected above. The points along a line should have roughly the same intensity gradient direction, and fit well onto a straight line.

After identifying all candidate lines, they are paired up to form candidate femoral shaft contours. The lines are paired based on the following criteria:

- The width w_i between a pair i of lines should fall within an acceptable range. From 200 training samples of femur images, it is found that the width has a unimodal distribution which can be modeled by a Gaussian G_s with a mean μ_s of 44.64 pixels and a standard deviation σ_s of 4.67 (Figure 4.4). So, given the width w_i, the probability that the pair of lines is the shaft contour is given by $G_s(w_i|\mu_s, \sigma_s)$.

Figure 4.3: Candidate shaft starting points.

- The lines in a pair i have the correct intensity gradient directions. Specifically, the intensity gradient of the line on the left of the femur should change from dark to bright along the positive x-axis, and that of the line of the right of the femur should change in the opposite direction (Figure 4.5). Moreover, they should also have large intensity gradient magnitudes M_i, which is computed as the mean of the intensity gradient magnitudes of the points along the lines.

- Thus, the probability P_i that a pair i of lines is indeed the shaft contour is proportional to the product $M_i G_s(w_i|\mu_s, \sigma_s)$, assuming the intensity gradient magnitude and the shaft width are independent factors. The intensity

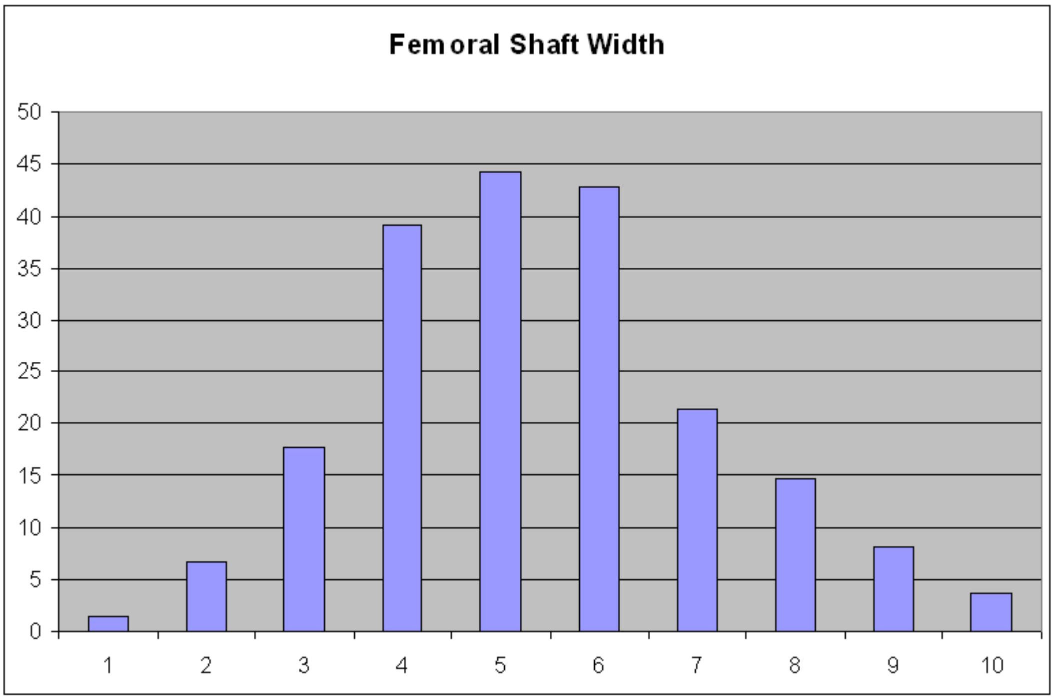

Figure 4.4: Femoral shaft width distribution obtained from 200 training samples. The width ranges from 31.82 pixels to 57.84 pixels. This range is equally divided into 10 bins. The y-axis is the number of samples falling in each bin.

gradient magnitude is based on x-ray absorption whereas the shaft width is based on the patient's body size. These two factors are thus independent.

So, each candidate femoral shaft i is associated with a probability measure P_i. The top candidates, at most three, with the largest probability measures are kept. Figure 4.6 illustrates an example with two candidate femoral shaft contours.

4.3.2 Detection of Candidate Femoral Heads

The femoral head is approximately circular. Usually, the contour of the femoral head is not very distinctive. On the other hand, the femur socket of the hip bone

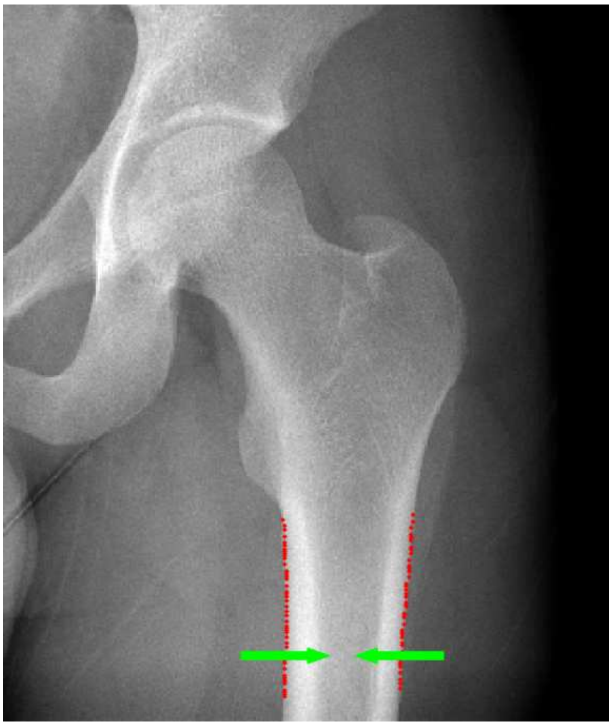

Figure 4.5: Gradient directions of shaft lines.

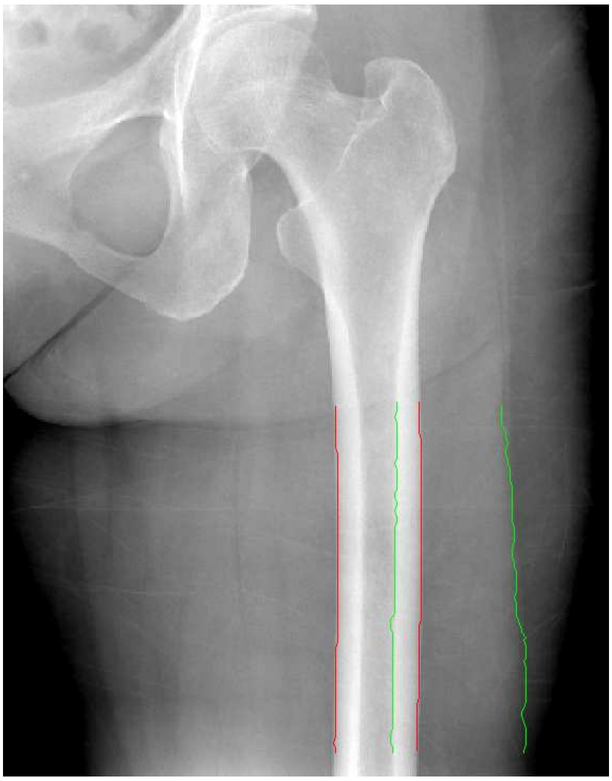

Figure 4.6: Candidate femoral shafts. The red pair is the first option and the green one is the second.

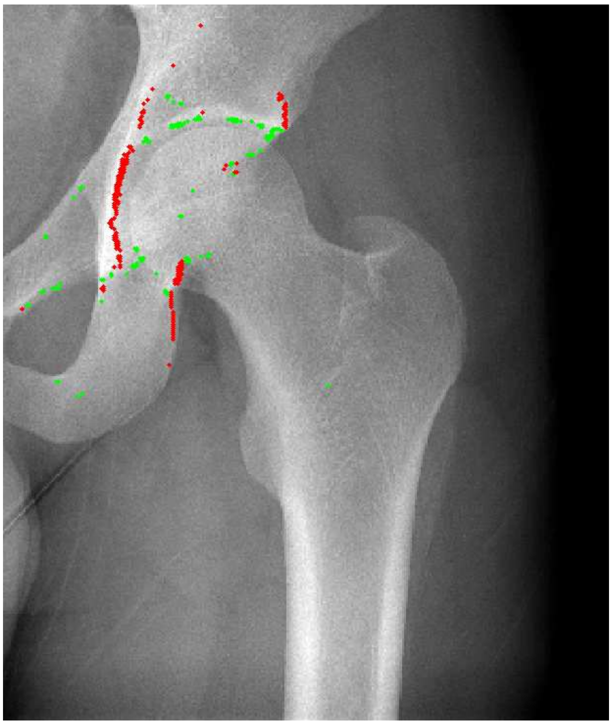

Figure 4.7: Strong edge points around the femoral head. The red and green dots have large horizontal and vertical intensity gradient components respectively.

appears as strong edges in x-ray images, and the points on these strong edges have very large horizontal or vertical intensity gradient components. So, such points are detected at the top left corner of the femur region in the image. Next, circles are fitted over these points using circular Hough transform.

For a particular patient, the size of the femoral head is positively related to that of the femoral shaft. From 200 training samples of femur images, it is found that the ratio of the radius of the femoral head to the width of the femoral shaft has a unimodal distribution which can be modeled by a Gaussian G_h with a mean μ_h of 0.91 and a standard deviation σ_h of 0.11 (Figure 4.8). Given a fitted circle i with radius r_i and a candidate shaft with width w_i, the probability that circle

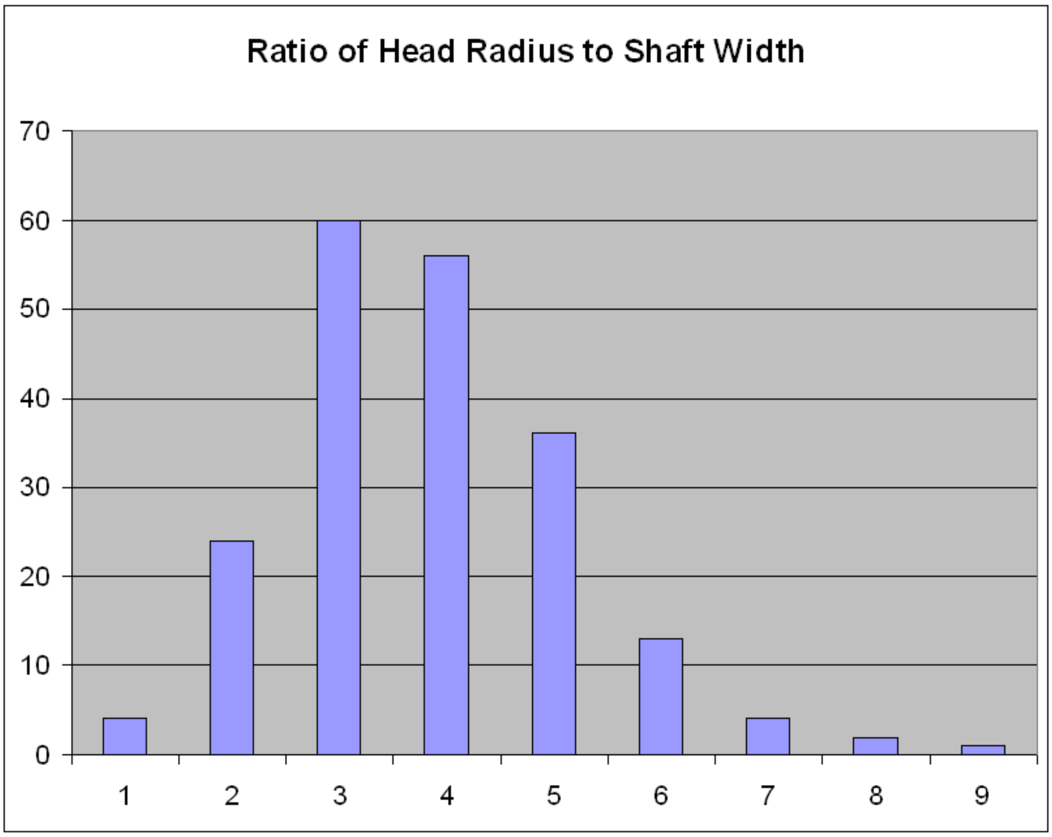

Figure 4.8: Distribution of the ratio of head radius to shaft width obtained from 200 training samples. The ratio ranges from 0.63 pixel to 1,39 pixels. This range is equally divided into 9 bins. The y-axis is the number of samples falling in each bin.

i falls onto the femoral head is given by $G_h(r_i/w_i|\mu_h, \sigma_h)$. For each candidate shaft found in the previous step, the top femoral head candidates, at most three, with the largest probabilities are kept. This produces at most nine shaft-head combinations. Fig. 4.9 illustrates an example with 3 candidate femoral heads.

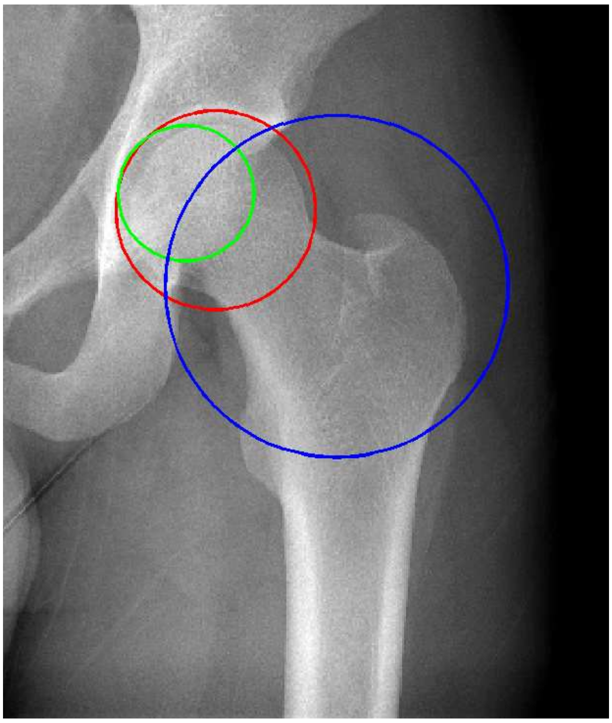

Figure 4.9: Candidate femoral heads.

4.3.3 Detection of Candidate Turning Points

In addition to the candidate femoral shafts and heads, an important feature point which we call the "turning point" is also extracted (Fig. 4.10). This feature point is located near the base of the greater trochanter, where the femur contour turns from concave to convex. It is obtained as follows:

- For each candidate femoral shaft, the line on the right side of the parallel pair is extended upward using contour following method with the straight line condition relaxed. So, the line now traces a curve that goes along the boundary of the greater trochanter.

- Next the second derivatives of the points along the curve is computed. The locations of the zero crossings of the second derivatives are identified.

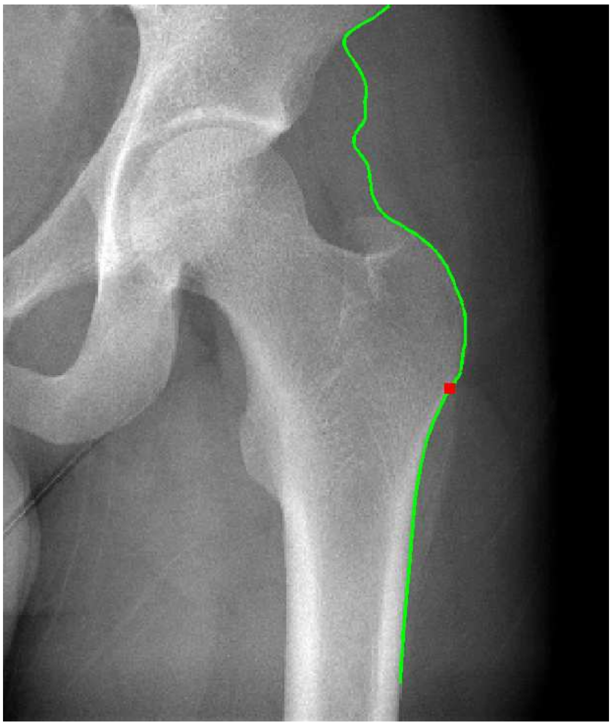

Figure 4.10: Turning point at great trochanter. The red dot denotes the turning point.

- For each shaft-head combination, the candidate turning points along the shaft and below the center of the head are identified.

- The lowest candidate turning points, at most three, are kept for each shaft-head combination. This produces at most 27 shaft-head-turning point combinations. The reason for keeping the lowest three candidates is that the bottom part of the image contains the shaft, which is quit straight. It is less likely to have many misleading candidates there.

4.3.4 Piecewise Registration of Femur Model

Figure 4.11(a) shows the model femur contour. For the automatic method the model contour does not contain the lesser trochanter because it does not contain important feature for fracture detection. As discussed in Section 4.1, the most important application of the automatic method is fracture detection. Including the lesser trochanter in the model is not useful for this purpose. Moreover, including the lesser trochanter will make the algorithm more complicated because it is not easy to detect it.

The model femur contour is divided by five feature points into five segments. The corresponding features points in the image are obtained as follows. The two feature points on the head contour are obtained from the top-most and left-most points of a candidate femoral head. The two feature points at the bottom of the shaft contour are obtained from a candidate femoral shaft. The last feature point is a candidate turning point.

The model femur contour is placed onto the image by piecewise registration of the segments based on each of the 27 possible shaft-head-turning point combinations. Each segment of the model femur contour is registered as follows. Let $\mathbf{u}_i$ and $\mathbf{u}_{i+1}$ be two neighboring feature points in the image. Let $\mathbf{u}'_i$ and $\mathbf{u}'_{i+1}$ be their corresponding feature points in the model femur contour respectively. Let $\mathbf{v} = \mathbf{u}_{i+1} - \mathbf{u}_i$ and $\mathbf{v}' = \mathbf{u}'_{i+1} - \mathbf{u}'_i$. The scaling factor s is given by

$$s = \frac{\|\mathbf{v}\|}{\|\mathbf{v}'\|} \tag{4.1}$$

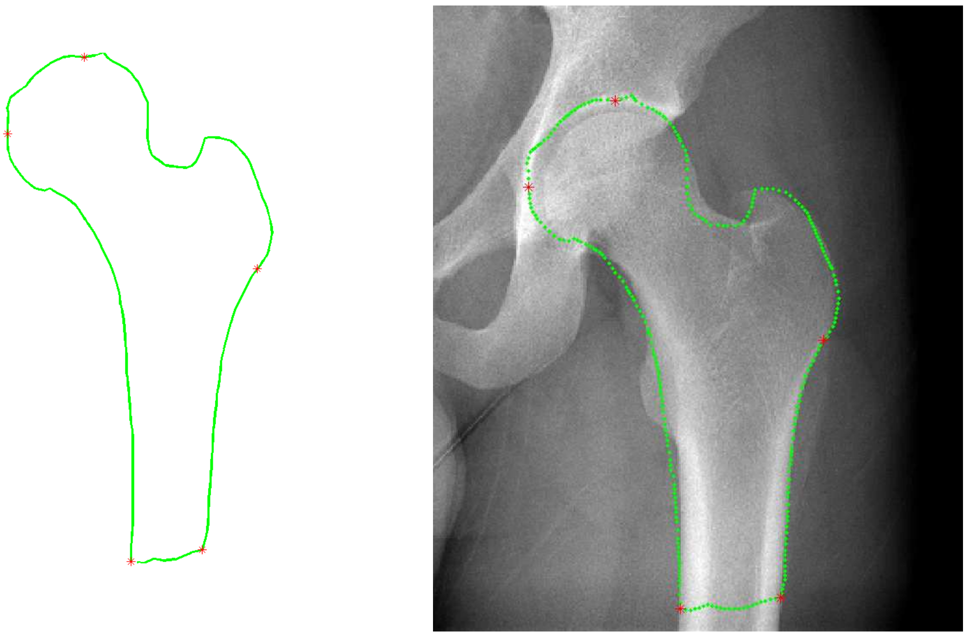

(a) (b)

Figure 4.11: Piecewise registration of femur model. (a) Model femur contour is divided by 5 feature points (red dots) into 5 segments. (b) Piecewise registered femur model used as the initial configuration of the snake algorithm.

and the rotation matrix $\mathbf{R}$ can be obtained by solving the equation

$$\mathbf{v} = s\mathbf{R}\mathbf{v}'. \tag{4.2}$$

Then for any point $\mathbf{p}'$ on the segment between $\mathbf{u}'_i$ and $\mathbf{u}'_{i+1}$, its registered position in the image, $\mathbf{p}$, can be computed as:

$$\mathbf{p} = s\mathbf{R}(\mathbf{p}' - \mathbf{u}'_i) + \mathbf{u}_i. \tag{4.3}$$

Figure 4.11(b) illustrates a model femur contour that is registered onto the image and to be used as the initial configuration of the active contour algorithm.

4.4 Active Contour with Curvature Constraints

In the semi-automatic method, the normal snake can accurately extract the femur contour because users already initialize the snake very close to the true femur contour. But in the automatic method, the piecewise registration results are not as close to the true femur contour as the users inputs. So there must be some shape constraints to guide the snake to snap to the true femur contour. As proposed by Ee et al. [Ee04], the shape of a snake can be constrained by constraining its curvature. The curvature of a contour is proportional to the rate of change of the tangent of the contour, which is a second derivative of the contour point. So, the curvature can be represented by the second derivative vector $\mathbf{v}''(s) = (x''(s), y''(s))$.

To constrain the curvature, a spring force is introduced. It is proportional to the difference between the actual curvature $\mathbf{v}''(s)$ of the snake and the reference curvature $\boldsymbol{\omega}(s)$ of the model. Then, the spring energy $E_c(\mathbf{v}(s))$ is given by

$$E_c(\mathbf{v}(s)) = \frac{\xi}{2}\|\mathbf{v}''(s) - \boldsymbol{\omega}(s)\|^2 \tag{4.4}$$

where ξ is a constant parameter that controls the stiffness of the snake. The larger the ξ, the more stiff is the snake, and thus, the better is the snake in preserving its reference shape encoded by the reference curvature $\boldsymbol{\omega}(s)$.

The snake's total energy E_{snake} changes from Equation 3.4 to

$$E_{snake} = \int [E_{int}(\mathbf{v}(s)) + E_c(\mathbf{v}(s)) + E_{image}(\mathbf{v}(s))]\, ds\,. \tag{4.5}$$

When E_{snake} is minimized, $\mathbf{v}(s)$ satisfies the following Euler-Lagrange equation, which can be obtained using variational calculus:

$$-(\alpha \mathbf{v}'(s))' + (\beta \mathbf{v}''(s))'' + (\xi \mathbf{v}''(s) - \xi \boldsymbol{\omega}(s))'' + \nabla E(\mathbf{v}(s)) = 0\,. \tag{4.6}$$

Denote the vectors $\nabla E = \mathbf{F} = (F_x, F_y)$ and $\boldsymbol{\omega} = (\omega_x, \omega_y)$. Discretizing Eq. 4.6 and rewriting in matrix form yields

$$\begin{aligned} \mathbf{A}_x \, \mathbf{x} + \mathbf{F}_x &= 0 \\ \mathbf{A}_y \, \mathbf{y} + \mathbf{F}_y &= 0\,. \end{aligned} \tag{4.7}$$

Let the snake be a closed contour with n points such that $\mathbf{v}(n+1) = \mathbf{v}(1)$. Then, the matrix $\mathbf{A}_x$ is given by

$$\mathbf{A}_x = \begin{bmatrix} c_1 & d_1 & e_1 & 0 & \cdots & 0 & a_1 & b_1 & f_1 \\ b_2 & c_2 & d_2 & e_2 & 0 & \cdots & 0 & a_2 & f_2 \\ \vdots & \vdots & \vdots & \vdots & \vdots & \vdots & \vdots & \vdots & \vdots \\ d_n & e_n & 0 & \cdots & 0 & a_n & b_n & c_n & f_n \\ 0 & 0 & 0 & 0 & \cdots & 0 & 0 & 0 & 1 \end{bmatrix} \tag{4.8}$$

where

$$\begin{aligned} a_i = e_i &= \beta + \xi \\ b_i = d_i &= -\alpha - 4\beta - 4\xi \\ c_i &= 2\alpha + 6\beta + 6\xi \\ f_i &= \xi(-\omega_{x,i-1} + 2\omega_{x,i} - \omega_{x,i+1})\,. \end{aligned} \tag{4.9}$$

Compared to the original snake, $\mathbf{A}_x$ has an additional column of constants f_i that capture the second derivatives of the reference curvature at points $\mathbf{v}(i)$. Moreover, an extra row of n zeros followed by a 1 is added to make the matrix square and invertible. The matrix $\mathbf{A}_y$ is the same as $\mathbf{A}_x$ except ω_x in f_i is replaced by ω_y.

Equation 4.7 can be solved iteratively by regarding $\mathbf{x}$ and $\mathbf{y}$ as functions of time t:

$$
\begin{aligned}
\mathbf{A}_x \mathbf{x}(t) + \mathbf{F}_x(t-1) &= -\gamma(\mathbf{x}(t) - \mathbf{x}(t-1)) \\
\mathbf{A}_y \mathbf{y}(t) + \mathbf{F}_y(t-1) &= -\gamma(\mathbf{y}(t) - \mathbf{y}(t-1))
\end{aligned}
\tag{4.10}
$$

where γ is a small constant time step. Rearranging the terms yields the iterative update equations:

$$
\begin{aligned}
\mathbf{x}(t) &= (\mathbf{A}_x + \gamma\mathbf{I})^{-1}(\gamma\mathbf{x}(t-1) - \mathbf{F}_x(t-1)) \\
\mathbf{y}(t) &= (\mathbf{A}_y + \gamma\mathbf{I})^{-1}(\gamma\mathbf{y}(t-1) - \mathbf{F}_y(t-1))\,.
\end{aligned}
\tag{4.11}
$$

The constrained snake algorithm is applied onto each of the candidate shaft-head-turning point combinations. After the snake algorithm has converged, the shape difference E_{sh} between the candidate resultant snake and the reference model is computed in terms of the mean squared error of rigid registration between them. As most femurs, especially those without severe shape distortion, are quite similar, a good extraction result should be quite similar to the model femur, which means minimizing E_{sh}. The mean M_g of the intensity gradient magnitudes of all the points along the candidate result contour is also computed. As most of the true femur contours are relative strong edges in x-ray images, a good extraction result should maximize this M_g. So the candidate result with the smallest E_{sh}/M_g is regarded as the extracted femur contour.

4.5 Experiments and Discussion

A training set of 200 femur images with manually extracted contours were used to determine the shaft width model and the femoral head radius model. A different set of 172 femur images were used to test the contour extraction method. The size of all training and testing images was 297×348. A simple model femur is used by the algorithm to extract the femur contours in the test images. The error of an extracted contour is measured in terms of the mean error between the points on the extracted contour and their closest points on the manually marked contour. Success rate is the fraction of testing samples whose femur contours are extracted accurately. A femur contour is considered successfully extracted if the error is less than 8 pixels, which is only 2% of the image size.

Of the 172 testing samples, 81.4% of the femur contours were successfully extracted. The mean and standard deviation of the error of the successful samples are 3.88 pixels and 1.50 pixels. Some successful results are shown in Figure 4.12.

Among the failed cases, 31.3% are such that at least one of the candidate solution is an acceptable solution but not the top ranking solution (e.g., Figure 4.13a). If we consider these cases (5.8% of total testing cases) as successful cases as well, then the success rate becomes 87.2%.

The other 68.7% of the failed cases do not have acceptable results among the candidate results. Failed samples are either fracture cases such as Figure 4.13(b) (5.8% of total testing cases) or healthy femurs with odd shapes such as Figure 4.13(c) (4% of total testing cases) or images that contain artifacts such as extraneous straight lines caused by analogue imaging process (Figure 4.13d) (3% of total testing cases). Healthy femurs with odd shape have very short neck or shaft or both, due to the unusual standing postures of the patients with fractures on the other femurs.

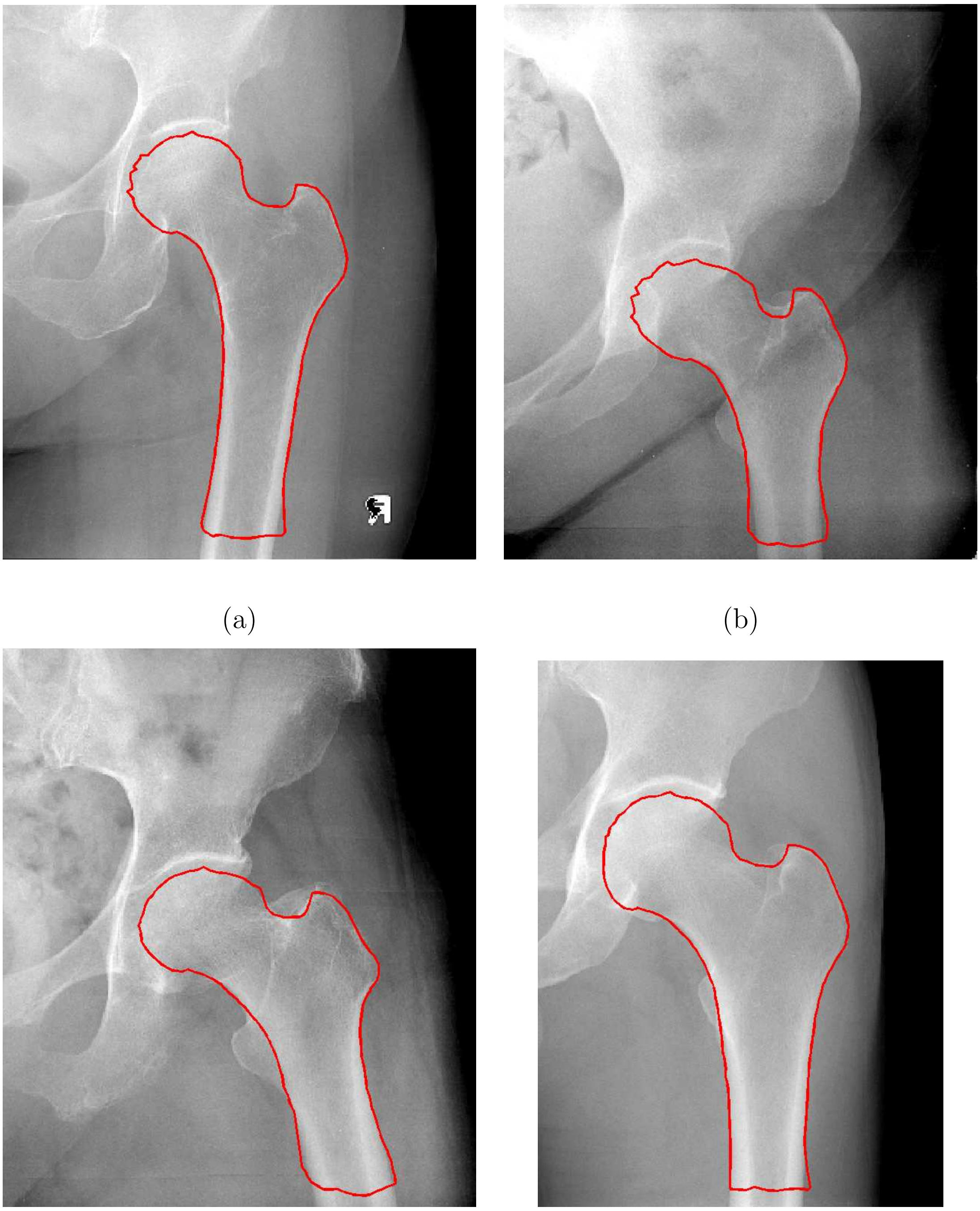

Figure 4.12: Sample test results. Despite the significant variations in the shapes, sizes, and orientations of the femurs in the images, correct femur contours are extracted. The errors are (a) 0.98 pixel, (b) 3.27 pixels, (c) 3.92 pixels and (d) 1.61 pixels.

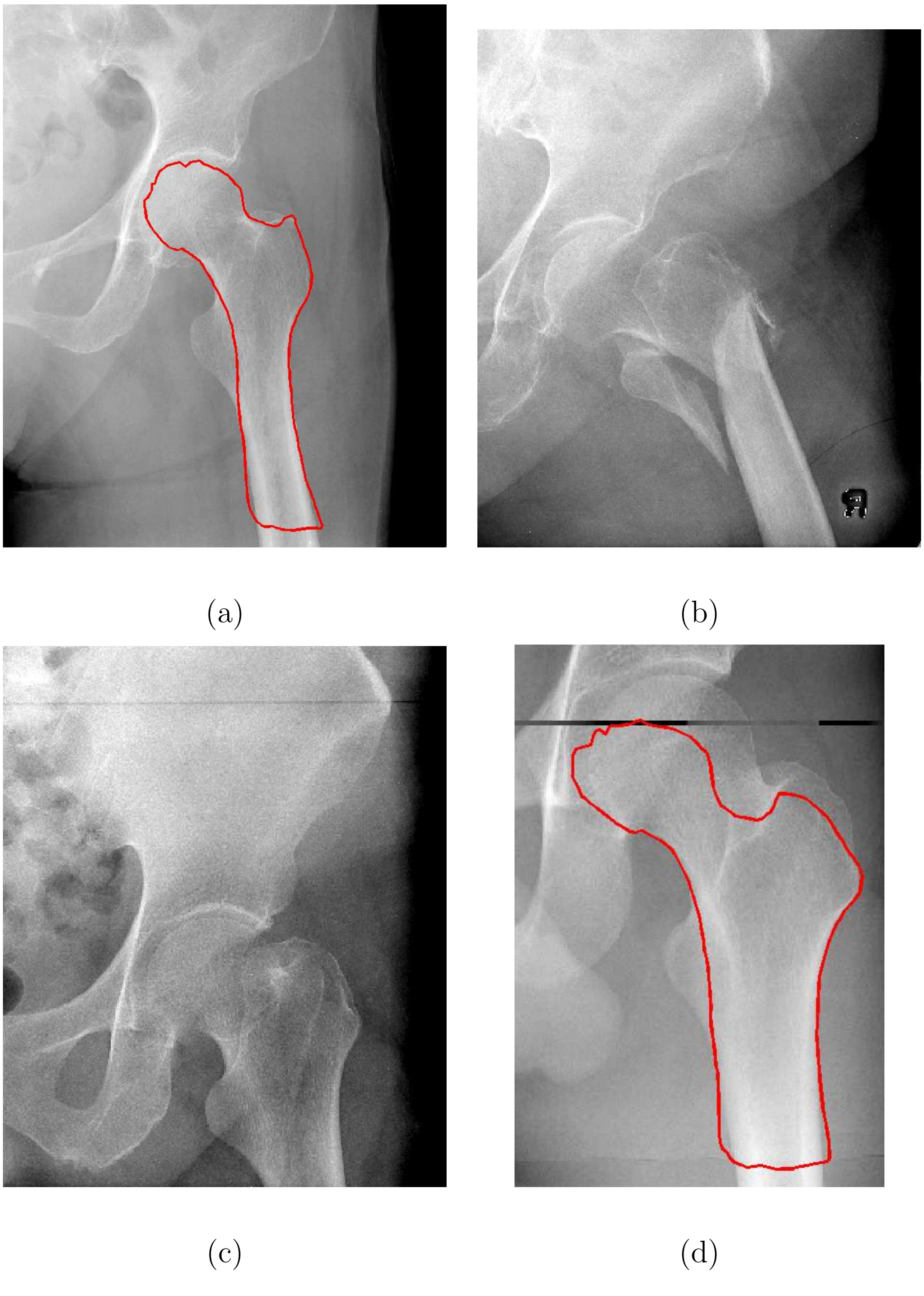

Figure 4.13: Sample failed cases. (a) One of the candidate solution is acceptable but not ranked at the top. (b) Fractured femur with severe shape distortion. (c) Healthy femur with an odd shape. There is almost no neck or shaft. (d) Image with extraneous straight line caused by analogue imaging process.

The comparison between the semi-automatic and automatic results shows that for some successful cases whose automatic extraction is accurate, their automatic results can be very close to the semi-automatic results (Figure 4.14(a, b)), while for some other cases whose automatic extraction is not so accurate, the errors of the automatic extraction are larger than that of the semi-automatic extraction (Figure 4.14(c, d)). Large errors occur at the femoral head and the lesser trochanter. The edges caused by the sockets on the pelvic bones for the femoral heads are usually stronger than the actual edges caused by the femoral heads. So the contours at this part can be easily distracted by the socket. And as discussed in 4.3.4, the lesser trochanter is omitted in the model femur contour for automatic extraction. So, it cannot be detected by the automatic extraction method.

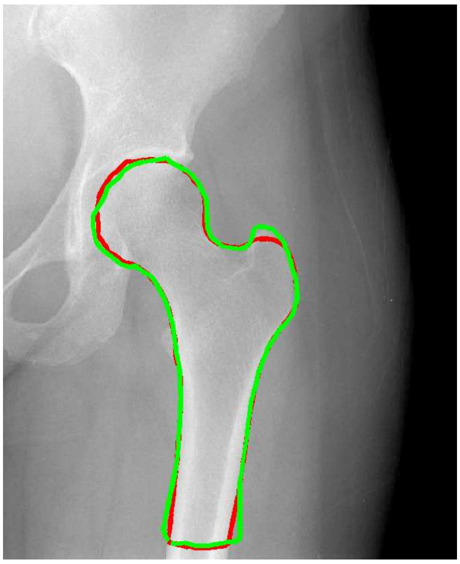

(a)

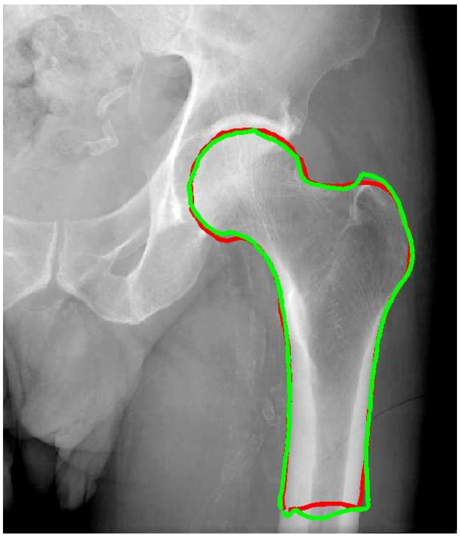

(b)

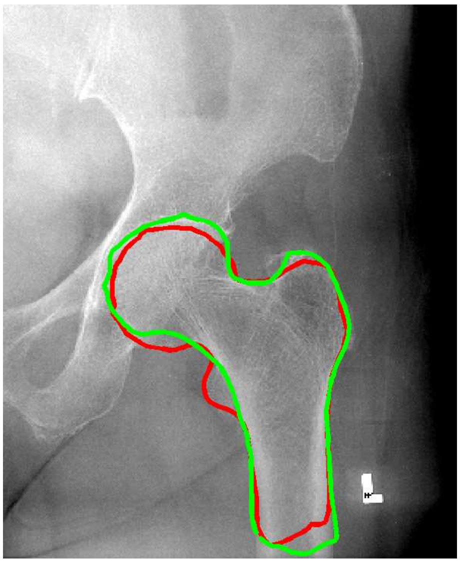

(c)

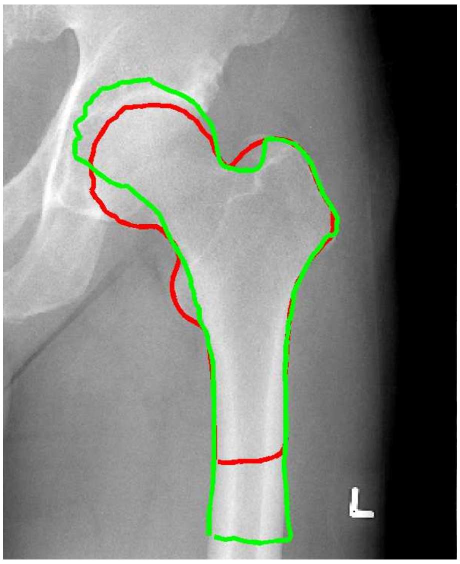

(d)

Figure 4.14: Comparison between semi-automatic results and automatic results. The red contours are the semi-automatic results and the green ones are the automatic results. The errors are (semi/auto): (a) 1.20/1.29 pixels, (b) 0.96/1.31 pixels, (c) 1.96/3.82 pixels, (d) 1.15/6.14 pixels.

Chapter 5

Future work

The automatic method fails mostly when the shapes of the femurs in the input images are very different from that of the model. To solve this problem, the model must be able to handle more shape variations. A possible solution is to incorporate some typical variations such as length of neck into the model. Another alternative solution is using more than one model. For each input image, every model can be used to extract the contour and the best result among the candidate solutions obtained from different models can be chosen.

But for severely fractured case, these two solutions cannot work. There is no way to get shape constraints for fractured cases because there are too many kinds of fractures. And due to the same reason, there is no way to build a model for fractured femurs. Automatic contour extraction of severely fractured femurs is very difficult to solve. However, if the contour extraction method can successfully handle all other shape variations except the variation caused by fractures, failing to extract the femur contour can imply that this femur is fractured. This failure can still solve the problem of fracture detection.

Another possible improvement is to use an atlas including the whole hip to guide the initialization. The atlas can provide the spatial relationship between the femur and other bones, which will make the initialization less sensitive to the extraneous edges caused by the muscles and bones. But as discussed in Section 2.4, the femur can be oriented differently due to the patients' standing posture. So the atlas must be able to handle articulation, which will make the atlas very complex and difficult to use.

This research work on contour extraction can also be extended to other body parts with long bones such as knees, ankles, wrists, etc. A general contour extraction method is very useful for medical image analysis applications.

Chapter 6

Conclusion

This thesis presented two methods for extracting femur contours from x-ray images. The semi-automatic method is useful when reliability and accuracy is more important. With this method, users inputs are used to align a model femur contour with the femur contour in x-ray image. Then, the active contour algorithm is applied to accurately identify the femur contour. The automatic method is needed when automation is more important. The method detects the position of the femoral shaft by finding pairs of roughly parallel straight lines at the bottom of the image. Then the method detects the position of the femoral head by best fitting the strong edge points with a circle. After that, the method detects the position of the turning point by locating the zero crossings of second derivatives along the right boundary of the shaft. According to these detected features, a model femur contour is registered piecewise to the x-ray image. Finally, active contour with shape constraints is applied to accurately identify the femur contour.

Experiments show that the semi-automatic method can always extract the femur contours very accurately. The automatic method can successfully extract the contours of femurs with regular shapes, despite the variations in size, shape and orientation. The accuracy of the successfully extracted contours from automatic method is good enough for fracture detection. The automatic method fails for severely fractured femurs, healthy femurs that appear to have odd shapes due to the patients' standing posture and images with artifacts due to analogue imaging process.

Bibliography

[AB94] R. Adams and L. Bischof. Seeded region growing. *IEEE Transactions on Pattern Analysis and Machine Intelligence*, 16(6):641–647, 1994.

[AM00] M. Stella Atkins and Blair T. Mackiewich. Fully automated hybird segmentation of the brain. In Issac N. Bankman, editor, *Handbook of Medical Imaging, Processing and Analysis*, chapter 11, pages 171–183. Academic Press, 2000.

[ANWD99] G. B. Aboutanos, J. Nikanne, N. Watkins, and B. M. Dawant. Model creation and deformation for the automatic segmentation of the brain in MR images. *IEEE Transaction on Biomedical Engineering*, 46(11):1346–1356, 1999.

[AOB03] E. B. Aksel, M. Ozkan, and O. Barlas. Atlas-guided neurosurgery. In *Proceeding International IEEE EMBS Conference on Neural Engineering*, pages 668–670, 2003.

[BC99] A. Bishnu and B. B. Chaudhuri. Segmentation of bangla handwritten text into characters by recursive contour following. In *Proceeding In-*

ternational Conference on Document Analysis and Recognition, pages 402–405, 1999.

[BHC93] J. C. Bezdek, L. O. Hall, and L. P. Clarke. Review of MR image segmentation techniques using pattern recognition. *Medical Physics*, 20:1033–1048, 1993.

[BJ88] P. J. Bsel and R. C. Jain. Segmentation through variable-order surface fitting. *IEEE Transactions on Pattern Analysis and Machine Intelligence*, 10(2):167–192, 1988.

[Can86] J. Canny. A computational approach to edge detection. *IEEE Transactions on Pattern Analysis and Machine Intelligence*, 8(6):679–698, 1986.

[Cel90] M. Celenk. A color clustering technique for image segmentation. *Computer Vision, Graphics, and Image Processing*, 52:145–170, 1990.

[CHTH94] T. F. Cootes, A. Hill, C. J. Taylor, and J. Haslam. Use of active shape model for locating structures in medical images. *Image Vision Computing*, 12:355–365, 1994.

[CHV+97] J. Chang, G. Han, J. M. Valverde, N. C. Griswold, J. F. Duque-Carrillo, and E. Sanchez-Sinencio. Cork quality classification system using a unified image processing and fuzzy-neural network methodology. *IEEE Transactions on Neural Networks*, 8(4):964–974, 1997.

[CJ04] H. Chen and A. K. Jain. Tooth contour extraction for matching dental radiographs. In *Proceeding International Conference on Pattern Recognition*, pages 522–525, 2004.

[CYL+04] Y. Chen, W.-H. Yap, W. K. Leow, T. S. Howe, and M. A. Png. Detecting femur fractures by texture analysis of trabeculae. In *Proceeding International Conferece on Pattern Recognition*, 2004.

[DMS99] Y. Deng, B. S. Manjunath, and H. Shin. Color image segmentation. In *Proceeding IEEE Conference on Computer Vision and Pattern Recognition*, 1999.

[Ee04] X. Ee. Shape-preserving elastic snakes. Department of Computer Science, School of Computing, National University of Singapore, 2004. Honour Year Project Report.

[FCH03] A. Foulonneau, P. Charbonnier, and F. Heitz. Geometric shape priors for region-based active contours. In *Proceeding International Conference on Image Processing*, volume 3, pages 413–416, 2003.

[GBBH96] P. Gibbs, D. L. Buckley, S. J. Blackband, and A. Horsman. Tumour volume detection from MR images by morphological segmentation. *Physcal Medicine and Biology*, 41:2437–2446, 1996.

[GDP+98] A. F. Goldszal, C. Davatzikos, D. L. Pham, M. X. H. Yan, R. N. Bryan, and S.M. Resnick. An image processing system for qualitative and quantitative volumetric analysis of brain images. *Journal of Computer Assisted Tomography*, 22:827–837, 1998.

[GKK98] Jean Gao, Akio Kosaka, and Avi Kak. A deformable model for human organ extraction. In *Proceeding International Conference on Image Processing*, volume 3, pages 323–327, October 1998.

[GMA+04] V. Grau, A. Mewes, M. Alcaniz, R. Kikinis, and S. Warfield. Improved watershed transform for medical image segmentation using prior information. *IEEE Transaction on Medical Imaging*, 23(4):447–458, 2004.

[HG00] G. Hamarneh and T. Gustavsson. Combining snakes and active shape models for segmenting the human left ventricle in echocardiographic images. *Computers in Cardiology*, pages 115–1118, 2000.

[HS85] R. M. Haralick and L. G. Shapiro. Image segmentation techniques. *Computer Vision, Graphics, and Image Processing*, 29(1):100–132, 1985.

[HZ01] P. He and J. Zheng. Segmentation of tibia bone in ultrasound images using active shape models. In *Proceeding International Conference of the IEEE Engineering in Medicine and Biology Society*, volume 3, pages 2712–2715, 2001.

[KGKW98] T. Kapur, W. E. L. Grimson, R. Kikinis, and W. M. Wells. Enhanced spatial priors for segmentation of magnetic resonance imagery. In

Proceeding Medical Imaging Computing and Computer-Assisted Intervention, pages 457–468, 1998.

[KWT88] M. Kass, A. Witkin, and D. Terzopoulos. Active contour models. *International Journal of Computer Vision*, 1:321–331, 1988.

[LHKU98] C. Lee, S. Hun, T.A. Ketter, and M. Unser. Unsupervised connectivity-based thresholding segmentation of midsaggital brain MR images. *Computers in Biology and Medicine*, 28:309–338, 1998.

[LKC+95] H. D. Li, M. Kallergi, L. P. Clarke, V. K. Jain, and R.A. Clark. Markov random field for tumor detection in digital mammagraphy. *IEEE Transaction on Medical Imaging*, 14:565–576, 1995.

[LNOK01] T. Lourens, K. Nakadai, H. G. Okuno, and H. Kitano. Graph extraction from color images. In *Proceeding European Symposium on Artificial Neural Networks*, pages 329–334, 2001.

[LNY00] W. N. Leung, C. M. Ng, and P. C. Yu. Contour following parallel thinning for simple binary images. In *Proceeding IEEE International Conference on Systems, Man, and Cybernetics*, pages 1650–1655, 2000.

[LS92] T. Lei and W. Sewchand. Statistical approach to X-Ray CT imaging and its applications in image analysis. *IEEE Transactions on Medical Imaging*, 11(1):62–69, 1992.

[LXC+04] S. E. Lim, Y. Xing, Y. Chen, W. K. Leow, T. S. Howe, and M. A. Png. Detection of femur and radius fractures in x-ray images. In *Pro-*

ceeding 2nd International Conference on Advances in Medical Signal and Information Processing, 2004.

[LZYZ04] P. Lin, F. Zhang, Y. Yang, and C. Zheng. Carpal-bone feature extraction analysis in skeletal age assessment based on deformable model. *Journal of Computer Science and Technology*, 2004.

[MA98] R. Malladi and J. A.Sethian. A real-time algorithm for medical shape recovery. In *Proceeding International Conference on Computer Vision*, pages 304–310, 1998.

[MFTM01] D. Martin, C. Fowlkes, D. Tal, and J. Malik. A database of human segmented natural images and its application to evaluating segmentation algorithms and measuring ecological statistics. In *Proceeding 8th International Conference Computer Vision*, pages 416–423, 2001.

[MRA04] D. P. Mukherjee, N. Ray, and S.T. Acton. Level set analysis for leukocyte detection and tracking. *IEEE Transactions on Image Processing*, 13(4):562–572, 2004.

[OBHF03] S. Ordas, L. Boisrobert, M. Huguet, and A. F. Frangi. Active shape models with invariant optimal features application to cardiac MRI segmentation. *Computers in Cardiology*, pages 633–636, 2003.

[PB00] J. Puzicha and S. Belongie. Model-based halftoning for color image segmentation. In *Proceeding International Conference on Pattern Recognition*, volume 3, pages 629–632, 2000.

[PBM03] H. Park, P. H. Bland, and C. R. Meyer. Construction of an abdominal probabilistic atlas and its application in segmentation. *IEEE Transaction on Medical Imaging*, 22(4):483–492, 2003.

[Per80] W. A. Perkings. Area segmentation of images using edge points. *IEEE Transactions on Pattern Analysis and Machine Intelligence*, 2(1):8–15, 1980.

[PHB99] J. Puzicha, T. Hofmann, and J. M. Buhmann. Histogram clustering for unsupervised image segmentation. In *Proceeding IEEE Conference on Computer Vision and Patter Recognition*, pages 602–608, 1999.

[PPO+96] S. Pohlman, K. A. Powell, N. A. Obuchowski, W. A. Chilcote, and S. Grundfest-Broniatowski. Quantitative classification of breast tumores in digitzed mamograms. *Medical Physics*, 23:1337–1345, 1996.

[Pra80] J. M. Prager. Extracting and labeling boundary segments in natural scenes. *IEEE Transactions on Pattern Analysis and Machine Intelligence*, 2(1):16–27, 1980.

[PXP00] D. L. Pham, C. Xu, and J. L. Prince. Current methods in medical image segmentation. *Annual Review of Biomedical Engineering*, 2:315–337, 2000.

[RM00] J. B. Roerdink and A. Meijister. The watershed tranform: Definitions, algorithms and parallelization strategies. *Foundmental Informaticae*, 41:187–228, 2000.

[RM03] X. F. Ren and J. Malik. Learning a classification model for segmentation. In *Proceeding International Conference on Computer Vision*, pages 10–17, 2003.

[Sch93] R. Schettini. A segmentation algorithm for color images. *Pattern Recognition Letters*, 14:499–506, 1993.

[Ser82] J. Serra. *Image Analysis and Mathematical Morphology.* Academic Press, 1982.

[Set96] J. A. Sethian. *Level Set Methods.* Cambridge University Press, 1996.

[SHC94] A. Sebbahi, A. Herment, and A. De Cesare. Automatic segmentation of ventricular endocardium on cine-CT images by an active contour process. In *Proceeding 16th Annual International Conference of the IEEE*, pages 522–523, 1994.

[SHD01] D. Shen, E. H. Herskovits, and C. Davatzikos. An adaptive-focus statistical shape model for segmentation and shape modeling of 3-D brain structures. *IEEE Transaction on Medical Imaging*, 20(4):257–270, 2001.

[SSW88] P. K. Sahoo, S. Soltani, and A. K. C. Wong. A survey of thresholding techniques. *Computer Vision, Graphics and Image Processing*, 41:233–260, 1988.

[STA96] P. P. Smyth, C. C. Taylor, and J. E. Adams. Automatic measurement of vertebral shape using active shape models. In *Proceeding IEEE Workshop on Applications of Computer Vision*, pages 176–180, 1996.

[Sur01] J. S. Suri. Two-dimensional fast magnetic resonance brain segmentation. *IEEE Engineering in Medicine and Biology Magazine*, 20(4):84–95, 2001.

[TCL+03] T. P. Tian, Y. Chen, W. K. Leow, W. Hsu, T. S. Howe, and M. A. Png. Computing neck-shaft angle of femur for x-ray fracture detection. In *Proceeding International Conference on Computer Analysis of Images and Patterns, LNCS 2756*, pages 82–89, 2003.

[Tia02] T. P. Tian. Detection of femur fractures in x-ray images. Master's thesis, Department of Computer Science, School of Computing, National University of Singapore, 2002.

[TPBF87] D. Terzopoulos, J. Platt, A. Barr, and K. Fleischer. Elastically deformable models. *Computer Graphics*, 21(4):205–214, 1987.

[TWK88] D. Terzopoulos, A. Witkin, and M. Kass. Constraints on deformable models : recovering 3D shape and nonrigid motion. *Artifitial Intelligence*, 36:91–123, 1988.

[WGKJ96] W. M. Wells, W. E. L. Grimson, R. Kikins, and F. A. Jolesz. Adaptive segmentation of MRI data. *IEEE Transaction on Medical Imaging*, 15(4):429–442, 1996.

[XP97] C. Xu and J. L. Prince. Gradient vector flow : A new external force for snakes. In *Proceeding of IEEE Conference on Computer Vision and Pattern Recognition*, pages 66–71, 1997.

[XSK+94] M. Xiao, Y. Q. Shi, D. Kristol, L. Horn, and P. Englet. Contour extraction from HVEM image of microvessel using active contour models. In *Proceeding 20th Annual Northeast Bioengineering Conference*, pages 1–2, 1994.

[YF03] P. J. Yim and D. J. Foran. Volumetry of hepatic metastases in computed tomography using the watershed and active contour algorithms. In *Proceeding IEEE Symposium on Computer-Based Medical Systems*, pages 329–335, 2003.

[ZBJ+98] H. Zhang, Z. Bian, D. Jiang, Z. Yuan, and M. Ye. Level set method for pulmonary vessels extraction. In *Proceeding International Conference on Image Processing*, volume 2, pages 1105–1108, 1998.

[ZTMR01] A. Zahour, B. Taconet, P. Mercy, and S. Ramdane. Arabic handwritten text-line extraction. In *Proceeding International Conference on Document Analysis and Recognition*, pages 281–285, 2001.